



**AFRL-RH-WP-TR-2013-
~~XXXX~~ AFRL-RH-WP-TR-2013-0079**

**Toxicity Evaluation of Engineered Nanomaterials:
Risk Evaluation Tools (Phase 3 Studies)**

**Saber Hussain
Christin Grabinski
Nicole Schaeublin
Elizabeth Maurer**

**Bioeffects Division
Molecular Bioeffects Branch**

**Mohan Sankaran
Case Western Reserve University**

**Ravindra Pandey
Michigan Technological University**

**Jerzy Leszczynski
Jackson State University**

**William Trickler
National Center for Toxicological Research/FDA**

January 2012

Final Report for Jan 2009 – Dec 2011

**DISTRIBUTION A: Approved for
public release; distribution unlimited,
AFRL-RH-WP-TR-2013-0079;
PA # 88ABW-2013-4073**

**DESTRUCTION NOTICE – Destroy by any method that will prevent disclosure of contents or
reconstruction of this document.**

**Air Force Research Laboratory
711th Human Performance Wing
Human Effectiveness Directorate
Bioeffects Division
Molecular Bioeffects Branch
Wright-Patterson AFB OH 45433-5707**

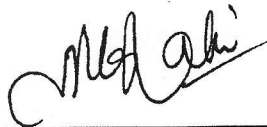
NOTICE PAGE

Using Government drawings, specifications, or other data included in this document for any purpose other than Government procurement does not in any way obligate the U.S. Government. The fact that the Government formulated or supplied the drawings, specifications, or other data does not license the holder or any other person or corporation; or convey any rights or permission to manufacture, use, or sell any patented invention that may relate to them.

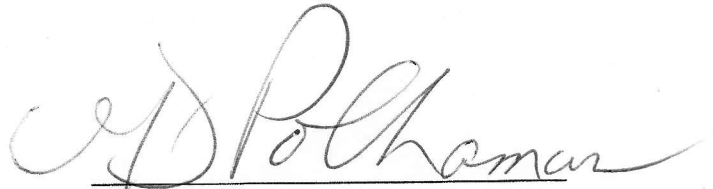
This report was cleared for public release by the 88th Air Base Wing Public Affairs Office and is available to the general public, including foreign nationals. Copies may be obtained from the Defense Technical Information Center (DTIC) (<http://www.dtic.mil>).

AFRL-RH-WP-TR-
2013-0079

THIS REPORT HAS BEEN REVIEWED AND IS APPROVED FOR PUBLICATION
IN ACCORDANCE WITH ASSIGNED DISTRIBUTION STATEMENT.



SABER HUSSAIN, Work Unit Manager
DAF Molecular Bioeffects Branch



GARRETT D. POLHAMUS, Dr-IV,
Bioeffects Division
Human Effectiveness Directorate
711th Human Performance Wing
Air Force Research Laboratory

This report is published in the interest of scientific and technical information exchange, and its publication does not constitute the Government's approval or disapproval of its ideas or findings.

REPORT DOCUMENTATION PAGE			Form Approved OMB No. 0704-0188		
Public reporting burden for this collection of information is estimated to average 1 hour per response, including the time for reviewing instructions, searching existing data sources, gathering and maintaining the data needed, and completing and reviewing this collection of information. Send comments regarding this burden estimate or any other aspect of this collection of information, including suggestions for reducing this burden to Department of Defense, Washington Headquarters Services, Directorate for Information Operations and Reports (0704-0188), 1215 Jefferson Davis Highway, Suite 1204, Arlington, VA 22202-4302. Respondents should be aware that notwithstanding any other provision of law, no person shall be subject to any penalty for failing to comply with a collection of information if it does not display a currently valid OMB control number. PLEASE DO NOT RETURN YOUR FORM TO THE ABOVE ADDRESS.					
1. REPORT DATE (DD-MM-YYYY) 30-01-2012		2. REPORT TYPE Final Tech Report		3. DATES COVERED (From - To) 1-21-2009 to 12-31-2011	
4. TITLE AND SUBTITLE Toxicity Evaluation of Engineered Nanomaterials: Risk Evaluation Tools (Phase 3 Studies)			5a. CONTRACT NUMBER		
			5b. GRANT NUMBER NA		
			5c. PROGRAM ELEMENT NUMBER 62202F		
6. AUTHOR(S) Saber Hussain; Christin Grabinski; Nicole Schaeublin; Elizabeth Maurer			5d. PROJECT NUMBER OAF		
			5e. TASK NUMBER WP		
			5f. WORK UNIT NUMBER OAFWP004		
7. PERFORMING ORGANIZATION NAME(S) AND ADDRESS(ES) 711 HPW/RHDJ 2729 R Street Wright-Patterson AFB OH 45433-5707			8. PERFORMING ORGANIZATION REPORT NUMBER		
9. SPONSORING / MONITORING AGENCY NAME(S) AND ADDRESS(ES) Air Force Materiel Command Air Force Research Laboratory 711th Human Performance Wing Human Effectiveness Directorate Bioeffects Division Molecular Bioeffects Branch Wright-Patterson AFB OH 45433-5707			10. SPONSOR/MONITOR'S ACRONYM(S) 711 HPW/RHDJ		
			11. SPONSOR/MONITOR'S REPORT NUMBER(S) AFRL-RH-WP-TR-2013-0079		
12. DISTRIBUTION / AVAILABILITY STATEMENT Distribution A: Approved for public release; distribution unlimited; PA#88ABW-2013-4142					
13. SUPPLEMENTARY NOTES					
14. ABSTRACT The overall objective was to develop a fundamental understanding of the interaction of engineered nanomaterials (NMs) with biological molecules that can be exploited to predict the toxicological effects and health risk in occupationally exposed humans. The specific objective was to develop the methodology to generate realistic NM airborne exposures, characterize NMs <i>in situ</i> , and estimate toxicity mechanisms and kinetics using predictive and computational models based on <i>in vitro</i> and <i>in vivo</i> data. The multiphase approach to this project involves consecutive and concurrent activities to develop a health risk evaluation system. We have successfully developed a realistic nanoaerosol exposure system that can be used to deposit NMs onto cells maintained at the air-liquid interface within a portable chamber for the investigation of NM toxicity. Future work will involve the routine investigation of NM toxicity using this system and correlation with traditional exposures.					
15. SUBJECT TERMS Engineered Nanomaterials, toxicity, airborne exposure					
16. SECURITY CLASSIFICATION OF:			17. LIMITATION OF ABSTRACT	18. NUMBER OF PAGES	19a. NAME OF RESPONSIBLE PERSON S. Hussain
a. REPORT U	b. ABSTRACT	c. THIS PAGE			19b. TELEPHONE NUMBER (include area code) NA
			SAR	56	

THIS PAGE INTENTIONALLY LEFT BLANK.

Front matter:

List of Tables

Table 1. Expected Deposited Concentration	15
Table 2. Mass Deposition Calculated using the MPPD Model	17
Table 3. Summary of Key Approaches Available for NM Aerosolization	19
Table 4. SMPS Data for the SSPD and VAG	21
Table 5. Specific Instrument Requirements for NM Aerosolization	24
Table 6. Symbols and Definitions of All Calculated Molecular Descriptors.....	30
Table 7. Crystallographic Data Utilized to Construct Metal Oxide Clusters.....	31
Table 8. Data on the Structure and Toxicity used in the Study.....	32
Table 9. List of Calculated Quantum - Mechanical Descriptors.....	42
Table 10. List of Calculated Image Descriptors	43
Table 11. Statistics for the Model's Coefficients	44

List of Figures

Figure 1. Schematic of the NM path and forces experienced in the chamber	3
Figure 2. Model geometry in Comsol.....	3
Figure 3. Velocity distribution through the chamber	4
Figure 4. Effect of NM size on particle trajectories	6
Figure 5. Effect of NM size on particle trajectories in an electric field	7
Figure 6. Time series of particle transport in an AC field.....	8
Figure 7. Picture of the experimental set-up for NP deposition experiments.....	9
Figure 8. Schematic of the flow in the set-up for NM deposition experiments.....	10
Figure 9. Electric fields that can be generated in the chamber.....	10
Figure 10. Characterization data for spherical gold nanoparticles.....	11
Figure 11. Deposition of gold nanoparticles aerosolized by electrospray.....	11
Figure 12. Number concentration of gold nanoparticles aerosolized by electrospray ...	12
Figure 13. Number size distribution of aerosolized NMs	13
Figure 14. Deposition of gold nanoparticles aerosolized by electrospray.....	13

Figure 15. Schematic of the relative size of the copper grids	14
Figure 16. Theoretical deposition of 10 nm gold nanoparticles in the respiratory tract..	16
Figure 17. Poster presented at the Society of Toxicology Annual Meeting	18
Figure 18. Image and operation schematics for aerosol generation instruments.	20
Figure 19. Al NMs aerosolized using the VAG and deposited onto TEM grids.....	22
Figure 20. Schematic for NM aerosol exposure using powder aerosolization	23
Figure 21. Multi-chamber model.....	25
Figure 22. Picture of the portable chamber set-up	26
Figure 23. Output screens on the humidity data logger	27
Figure 24. Alamar Blue assay	27
Figure 25. Williams plot describing applicability domains of GA-MLR model	33
Figure 26. Experimentally determined <i>versus</i> predicted log values of 1/EC ₅₀	34
Figure 27. Mechanism of electron transfer between the MeOx surface	38

Approach

Prior work developed a novel exposure chamber that produces NM aerosols and delivers them to cells at the air-liquid interface. This effort continues the development of a chamber that will provide the methodology necessary for generating realistic gas phase NM exposures, in addition to characterizing and assessing NM toxicity kinetics and mechanisms. An instrument that will characterize NMs *in situ* will be purchased and used to assess NMs generated in a previously developed chamber. This instrument was necessary for continuous monitoring of the test atmosphere to ensure well-characterized and systematic toxicity data that was useful for predictive modeling and risk assessment. This effort was expected to yield toxicological data for predictive modeling relevant to risk assessment.

A. Purchase a Scanning Mobility Particle Sizer and associated items

- *The Scanning Mobility Particle Sizer (SMPS) was used to determine the size distribution of aerosolized NMs. The SMPS uses an inertial impactor to remove large particles outside the measurement range, then passes the NMs through an ion neutralizer, which charges the particles and allows them to be separated using a Differential Mobility Analyzer. The NMs are then coated with a condensing liquid and counted using an optical detector in the Condensation Particle Counter. The sample can be drawn from the point of NM generation or from the exposure zone. SMPS spectrometers include Aerosol Instrument Manager software, which controls instrument operation and collects high resolution data.*
- *The Data Merge Software enables merging and fitting of SMPS and Aerosol Particle Sizer data files to create and display a wide particle size range from 0.0025 to 20 μm . The Aerosol Particle Sizer was used to measure sizes above the range of the Scanning Mobility Particle Sizer.*
- *The equipment requested will support in situ NM characterization, which was necessary for continuous monitoring of the test atmosphere to ensure well characterized and systematic toxicity data that were useful for predictive modeling and risk assessment.*

This was covered during the Expert Review conducted in August 2012.

B. Evaluate chamber generated nanomaterials

- *Characterize the size distribution of gas phased NMs produced via microplasma or electrospray using the SMPS*
- *Collect NMs on substrates for determination of material characteristics such as morphology and size distribution using electrostatic deposition via the Nanometer Aerosol Sampler*
- *Evaluate cell function and viability after exposure to NMs and study the kinetics of uptake and translocation of NMs in cellular systems using standardized in-house techniques*

The main objective of this study was to investigate the *in vitro* toxicity of aerosolized nanomaterials (NMs) with the goal of more accurately depicting inhalation exposure. There is a research gap in understanding NM aerosol deposition in a biologically-relevant environment, which is critical for relating dose and toxicological effects. The proposed approach is a more realistic exposure method than what is used for traditional nanotoxicology studies and poses unique challenges.

Due to the size of nanomaterials (NMs), they do not easily deposit out of a gas stream onto a substrate. One approach to overcome this challenge is to apply an electric force on the NMs, driving them to deposit at a controlled rate. This is a technique often used by industrial hygienists for characterizing aerosolized NMs in a field environment, but they use harsh air flow rates and direct current electric fields that cannot be sustained by the cells. Therefore, we must adapt this technology specifically for *in vitro* toxicology studies.

In order to investigate this subject in detail, we developed a multi-physics model incorporating an alternating current (AC) electric field and particle-filled air flow within the chamber. The model is designed after an experimental chamber that has been built for investigating the effect of frequency on NM deposition. The model will allow for many variations to be considered, which will reduce the amount of materials required for experimental investigations. The results of the simulations and experimental validations are expected to yield valuable information to support the dosimetry of aerosolized NMs for *in vitro* toxicology studies. The geometry is shown in Figure 1.

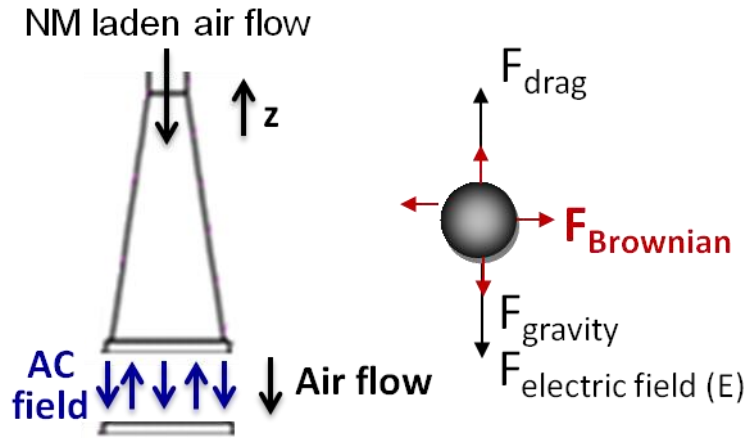


Figure 1. Schematic of the NM path and forces experienced in the chamber.

The geometry was modeled in Comsol based on the dimensions of the chamber and by defining an inlet velocity and zero pressure at the outlet (Figure 2).

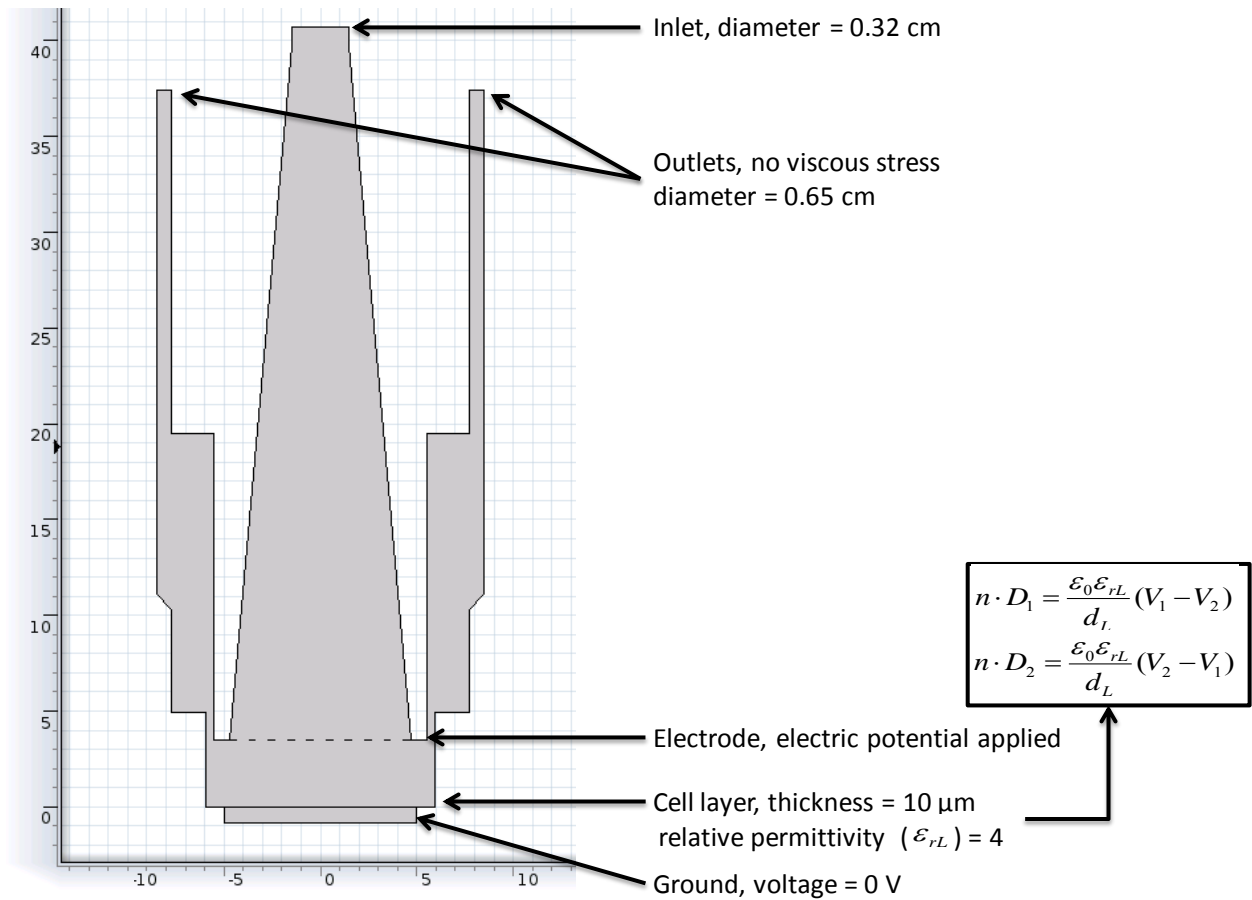


Figure 2. Model geometry in Comsol

DISTRIBUTION A: Approved for public release; distribution unlimited, PA# 88ABW-2013-4142

The velocity of particle filled air through the chamber was simulated using numerical analysis. The key assumptions include: incompressible Newtonian fluid (constant fluid density, constant fluid viscosity) and steady-state continuous flow. The governing equations include the continuity equation and momentum equations:

$$\text{Continuity equation:} \quad \nabla \vec{v} = 0 \quad (1)$$

where $\nabla \vec{v}$ is the gradient velocity vector.

$$\text{Momentum equation:} \quad \rho_f \vec{v}(\nabla \vec{v}) = -\nabla p + \mu \nabla^2 \vec{v} + \rho_f \vec{g} \quad (2)$$

where p is pressure, ρ_f is the fluid density, μ is fluid viscosity, and \vec{g} is the acceleration due to gravity. At the walls, the no slip condition was applied (equation 3).

$$\vec{v}_{wall} = 0 \quad (3)$$

where \vec{v}_{wall} is velocity vector at the boundary.

The temperature was assumed to be constant at 310.15 K. The value for density and viscosity were taken to be the values for air at 310.15 K.

The numerical procedure was performed for flow rate of 20 mL/min, which is feasible for experiments with cells. The results are shown in Figure 3 for 20 mL/min.

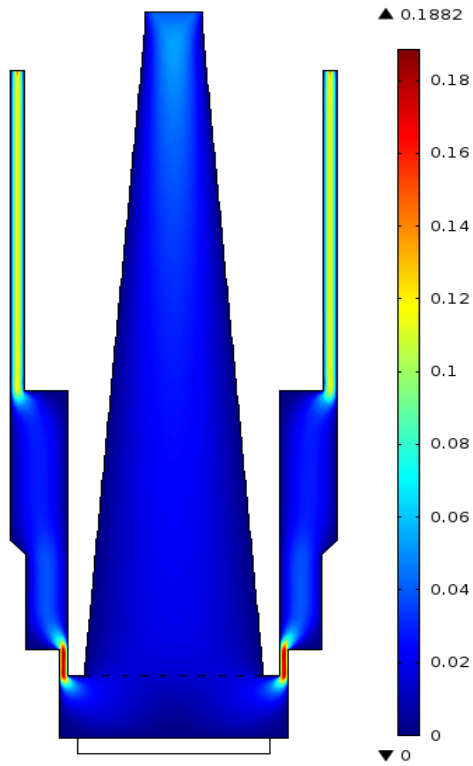


Figure 3. Velocity distribution through the chamber.

The velocity distributions developed in Figure 3 were used to solve for the particle trajectories in the time dependent domain. To calculate the particle trajectories over time, a force balance was created on each NP including the effects of Brownian motion, gravity, and drag force. The NP phase was assumed sufficiently dilute that particle-particle interactions are negligible. For each parameter, the NP trajectories were predicted. The equation of motion for a representative particle in the Lagrangian reference frame was used. In this approach, the particle inertia is equated with the forces on the particle. The general equation of motion arises from Newton's Second Law that mass times acceleration is equal to the net forces acting on the particle.

$$\frac{d\vec{v}_p}{dt} = \Sigma \vec{F} \quad (4)$$

where \vec{v}_p is the particle velocity.

Equation (4) simplifies to:

$$\Sigma \vec{F} = \vec{F}_{drag} + \vec{F}_{gravity} + \vec{F}_{Brownian} + \vec{F}_{electric} \quad (5)$$

The key forces on the NPs in a static environment include gravity and diffusion. However, in the dynamic condition, the momentum due to convection and drag force must be considered. For both conditions, the agglomerate size and density significantly affect the transport properties of NPs. Additionally, the Cunningham Correction Factor (C_c) must be considered, since the NP diameter (d_p) approaches the mean free path of air (λ).

$$C_c = 1 + \left(\frac{\lambda}{d_p}\right) \left\{ 2.514 + 0.8e^{\left(\frac{-55d_p}{\lambda}\right)} \right\} \quad (6)$$

The drag force describes resistance to the fluid. The drag force (\vec{F}_{drag}) and gravity force ($\vec{F}_{gravity}$) were computed as follows:

$$\vec{F}_{drag} = m_p \frac{18\mu}{C_c \rho_p d_p^2} (\vec{v} - \vec{v}_p) \quad (7)$$

$$\vec{F}_{gravity} = \rho_p g \frac{\pi d_p^3}{6} C_c \quad (8)$$

where m_p is the mass of the particle, ρ_p is the density of the particle, $(\vec{v} - \vec{v}_p)$ is the relative velocity of air to the particle, and g is the force of gravity.

For sub-micron particles, the effects of Brownian motion are included, and were modeled as white noise random process as described by Li and Ahmadi (1) using the following equation:

$$\vec{F}_{Brownian,i} = N_i \sqrt{\frac{S}{\Delta t}} \quad \text{where } S = \frac{216\mu k_B T}{\pi \rho_f^{-1} \rho_p^3 d_p^5 C_c} \quad (9)$$

where k_B is the Boltzmann's constant (1.38×10^{-23} J/K), T is the temperature (310.15 K), μ is the air viscosity and N_i is a zero-mean, unit variance normal random number and Δt is the simulation time step.

The electric force is calculated as shown below:

$$\vec{F}_{electric} = qZ\vec{E} \quad (10)$$

where q is the elementary charge (1.6×10^{-19} C/e⁻) and the trajectory calculations are based on the force balance on the particle, using the local continuous phase conditions as the particle moves through the flow. The momentum exchanges from the continuous phase to the discrete phase were computed by examining the change in momentum of the NP as it passes through each control volume in the model. During the motion of the NPs, we assumed that they did not exchange mass with the continuous phase, and they do not participate in any chemical reaction. When the NP makes contact with the cell layer, it is assumed to be trapped (frozen). The time step was set to 0.1 seconds, and the simulation was run for 20 seconds to allow for all of the NPs to travel through the system. The NP-filled air velocity was set to 20 mL/min. Results are shown in Figure 4.

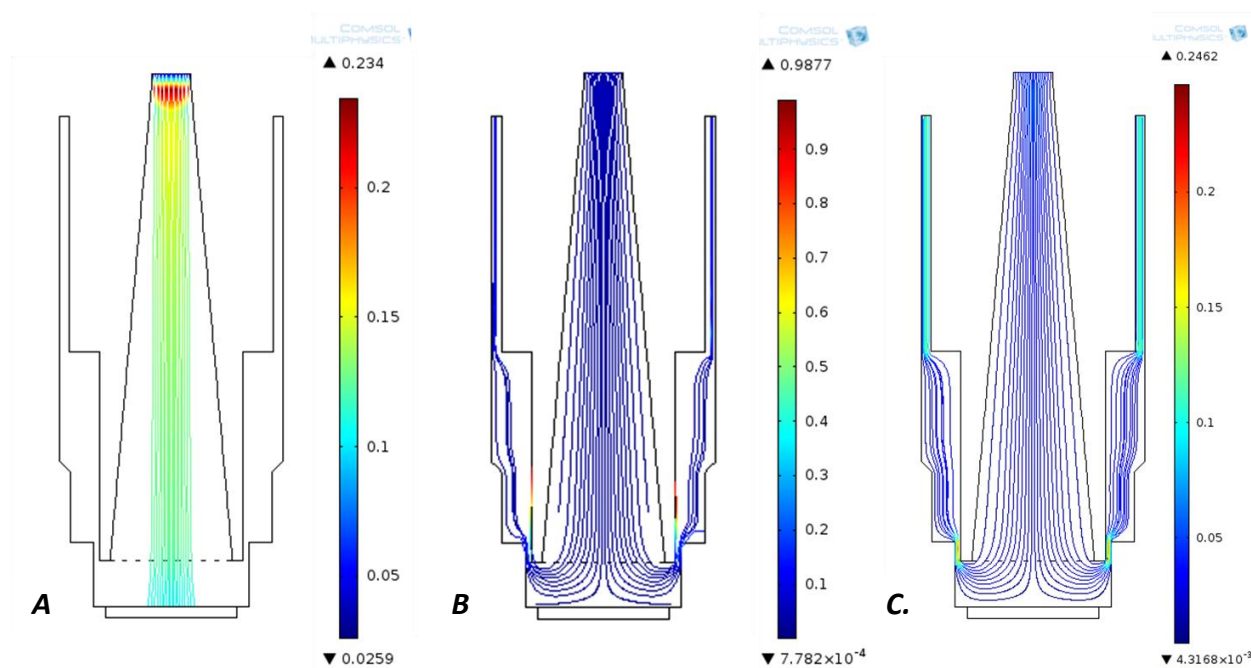


Figure 4. Effect of NM size on particle trajectories. A. 1 micron; B. 60 nm; C. 10 nm

The data shown in Figure 4 highlight the requirement for an external force to be applied for depositing NMs in the chamber, where 1 micron particles deposit due to impaction and 10 nm NMs remain completely aligned with the gas stream and do not deposit. It is important to note that the current applied in these high voltage fields is several orders of magnitude lower than that used for electroporation and is not expected to have an impact on the cells (2). The results for addition of an electric field are shown in Figure 5.

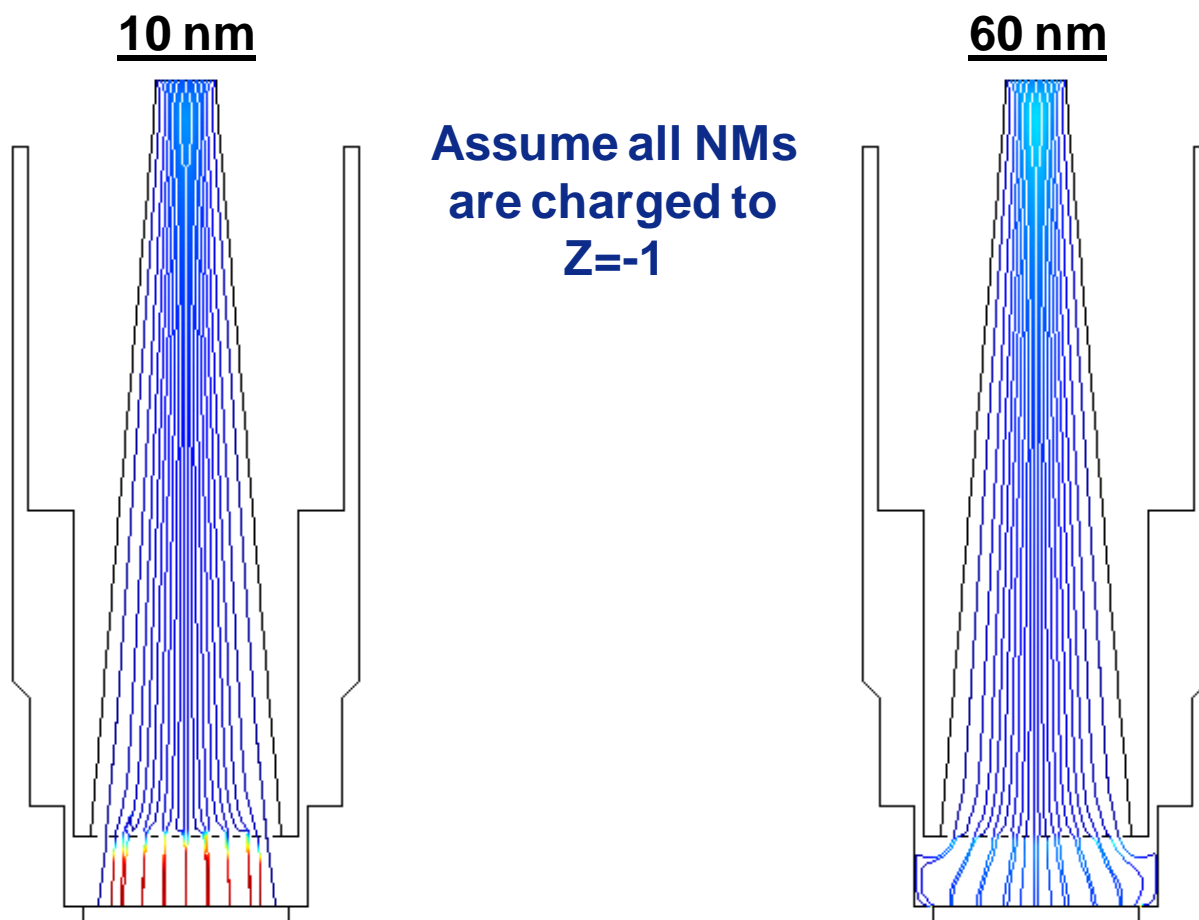


Figure 5. Effect of NM size on particle trajectories in an electric field (0.5 kV/cm).

The results show that an electric field can be used to force NM deposition and that a stronger electric field is required for increasing NM size. Savi and colleagues (2) suggested that an AC field (as opposed to a direct current (DC) field) is required when working with cells in order to avoid migration of charged species in the cell culture media during exposure. This idea provided the basis for implementing an AC field to apply a deposition force on NMs in the chamber.

It is well known that deposition is enhanced with increasing field strength, but the effect of frequency is not well understood. Due to the bipolar charge distribution on the NMs, the frequency must be controlled to apply an attracting force long enough to avoid opposing NMs from the substrate before switching polarity. A time series for NM transport in the chamber in the presence of an AC field is shown in figure 1. The flow rate was set to 20 mL/min, particle diameter 10 nm, and particle charge of -1. The particles should be repelled in a negative field and attracted to the cell surface in a positive field, which was verified by the model (figure 6).

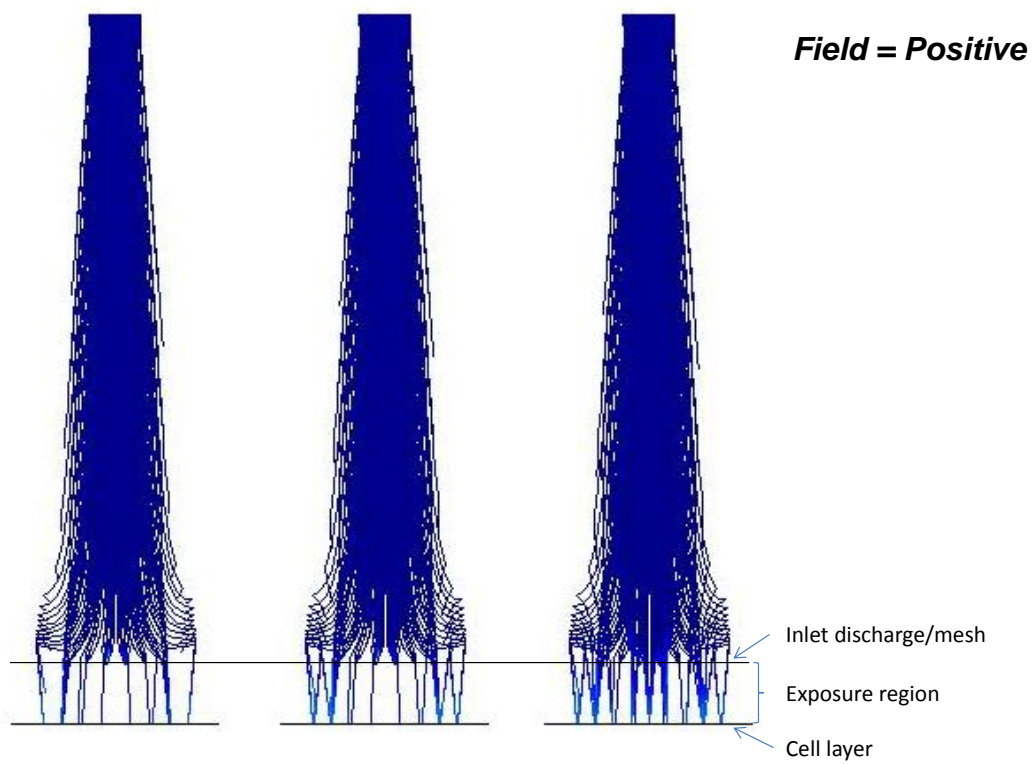
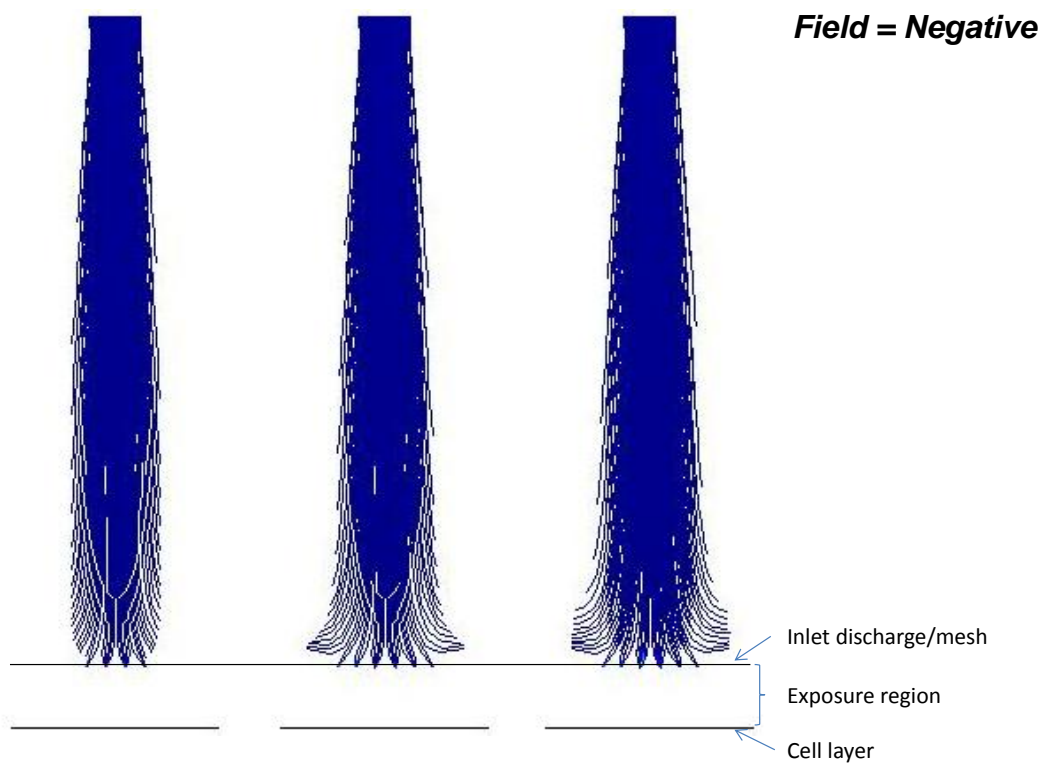


Figure 6. Time series of particle transport in an AC field (10 kV/cm, 1Hz) at 20 mL/min, 10 nm Au NPs, drag and gravity forces included, AC field, particle charge = -1.

The model shows that the particles are only attracted to the cell layer when the polarity is opposite of the NP charge, and that the particles are repelled when the polarity is the same as the NP charge. There are two proposed mechanisms for what the ultimate fate is for the NPs when the field polarity is opposite of the NP charge: (1) the charge is removed from the NP when it is repelled and hits the tube wall, allowing it to flow out of the chamber or (2) the NP is held in a repelled state and deposited when the polarity switches. The mechanism must be elucidated experimentally.

For preliminary dosimetry studies, a prototype chamber was used (modified horizontal diffusion chamber; see figure 7). NMs were aerosolized using electrospray, and deposition in the prototype chamber was characterized as a function of NM concentration and electric field properties. A function generator and high voltage amplifier were used to vary the electric field properties. The aerosol concentration was also characterized using a condensation particle counter (CPC). A picture of the set-up is shown in figure 7. A simplified schematic of the flow in the set-up is shown in figure 8. An image of different electric field shapes that can be generated within the chamber is shown in figure 9. It is not well-understood how these different shapes will affect NM deposition.



Figure 7. Picture of the experimental set-up for NM deposition experiments.

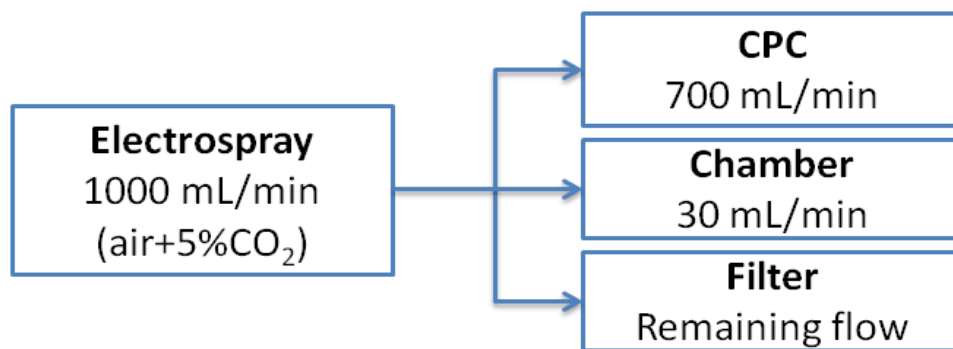


Figure 8. Schematic of the flow in the set-up for NM deposition experiments.

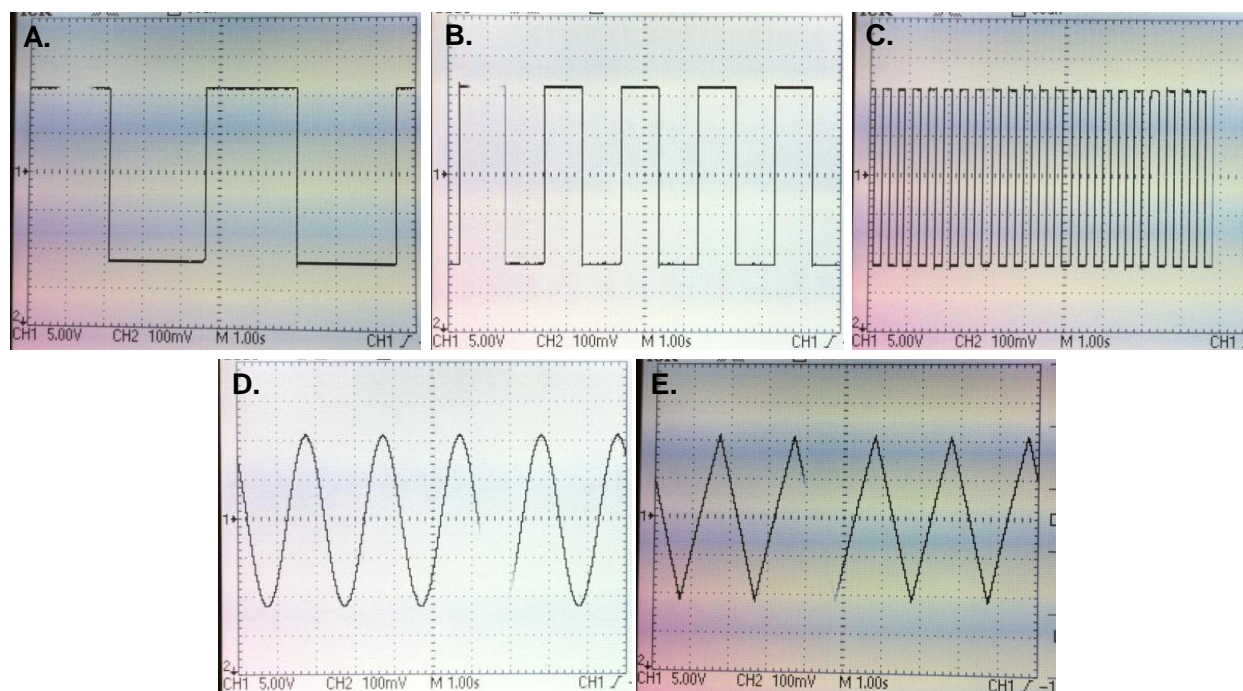


Figure 9. Electric fields that can be generated in the chamber A. Square wave, frequency 0.4 Hz; B. Square wave, frequency 1 Hz; C. Square wave, frequency = 5 Hz; D. Sine wave, frequency = 1 Hz; E. Sawtooth wave, frequency = 1 Hz.

The NMs aerosolized for this study were spherical gold nanoparticles synthesized using citrate reduction. The characterization data for these particles are shown in figure 10.

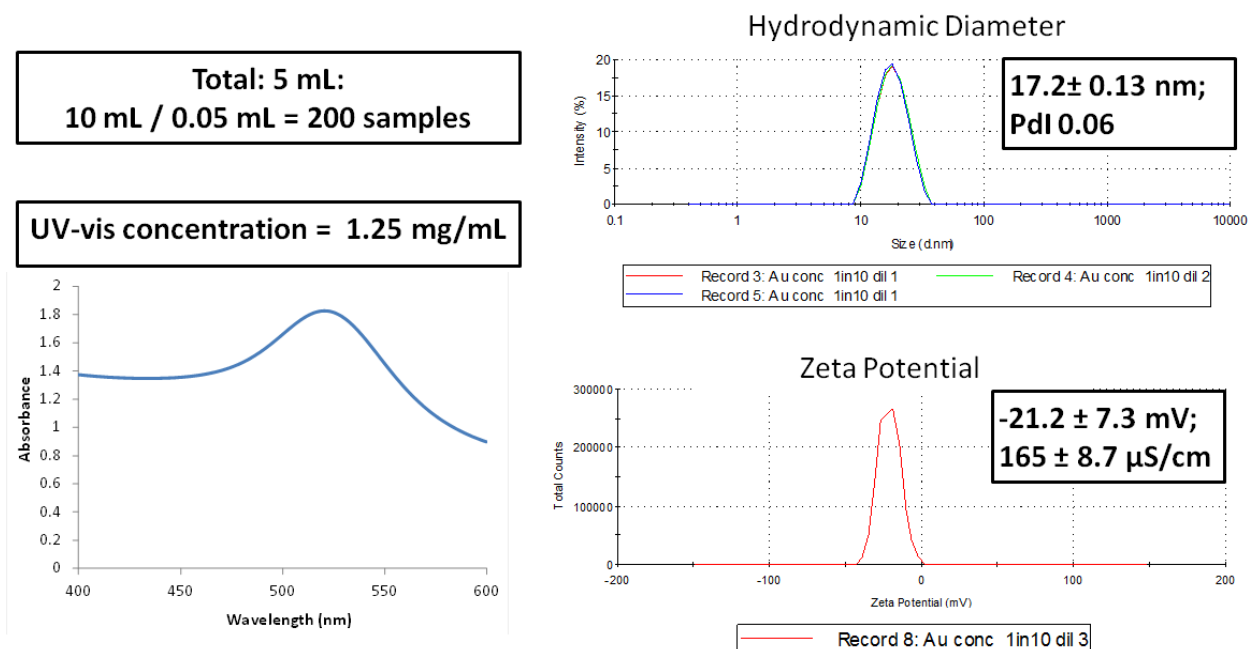


Figure 10. Characterization data for spherical gold nanoparticles.

For the first study, a concentration of 0.8 mg/mL was aerosolized. The deposition was carried out with AC electric field strength with a strength of 20 kV/cm and frequency of 0.4 Hz. Using these settings, the NMs appeared as large spherical agglomerates (figure 11).

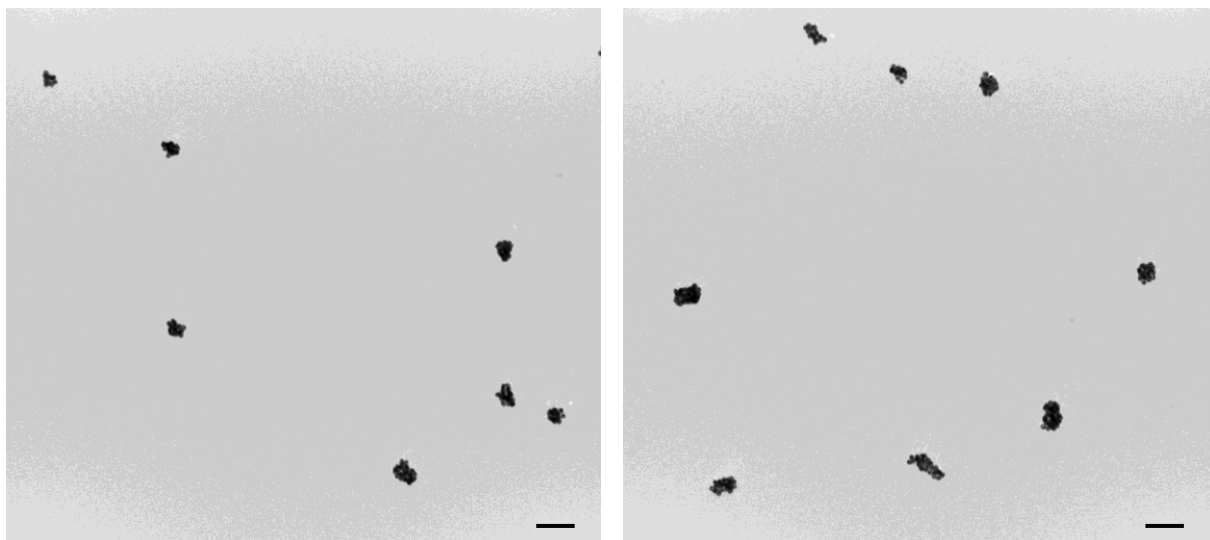


Figure 11. Deposition of gold nanoparticles aerosolized by electrospray with settings: 20 kV/cm and 0.4 Hz. The scale bar is equal to 100 nm.

In order to reduce the agglomerate size, the concentration of gold NMs was reduced to 100 µg/mL. At this reduced concentration, it was necessary to add fetal bovine serum proteins to achieve conductivity appropriate for electrospray (1%). The aerosol concentration was measured using CPC and found to remain consistent for the length of the experiment (figure 12).

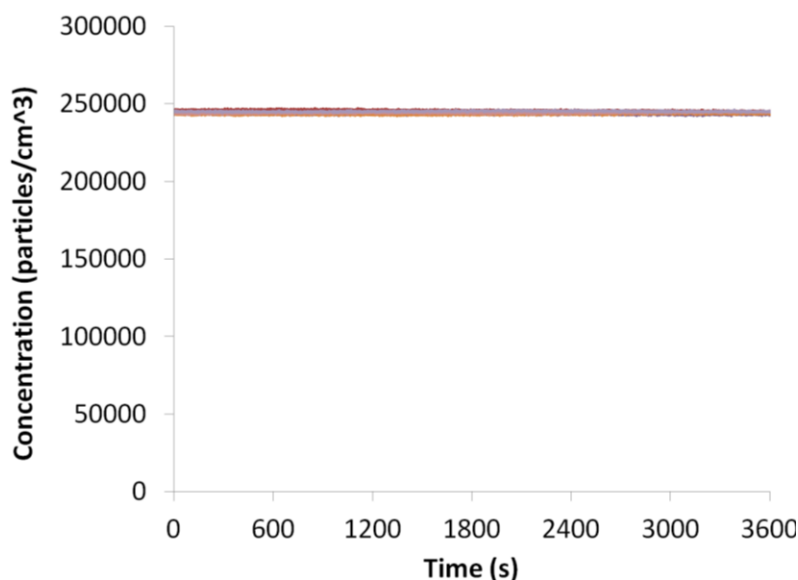


Figure 12. Number concentration of gold nanoparticles aerosolized by electrospray, measured using CPC.

The Nanoscan (TSI, inc.), which is a scanning mobility particle sizer (SMPS) capable of measuring the size distribution and concentration of aerosols was also used to characterize the NM aerosols. Experiments were conducted to investigate the effect of conductivity on the aerosolization of nanoparticles by electrospray (figure 13). The size distribution is bimodal for gold (Au) + fetal bovine serum when diluted in water and shifted to the right when diluted in citrate. The overall concentration increased with conductivity (in order of increasing conductivity: 1.4×10^4 ; 7.3×10^5 ; 1.1×10^6 ; 1.6×10^6 #/cm³).

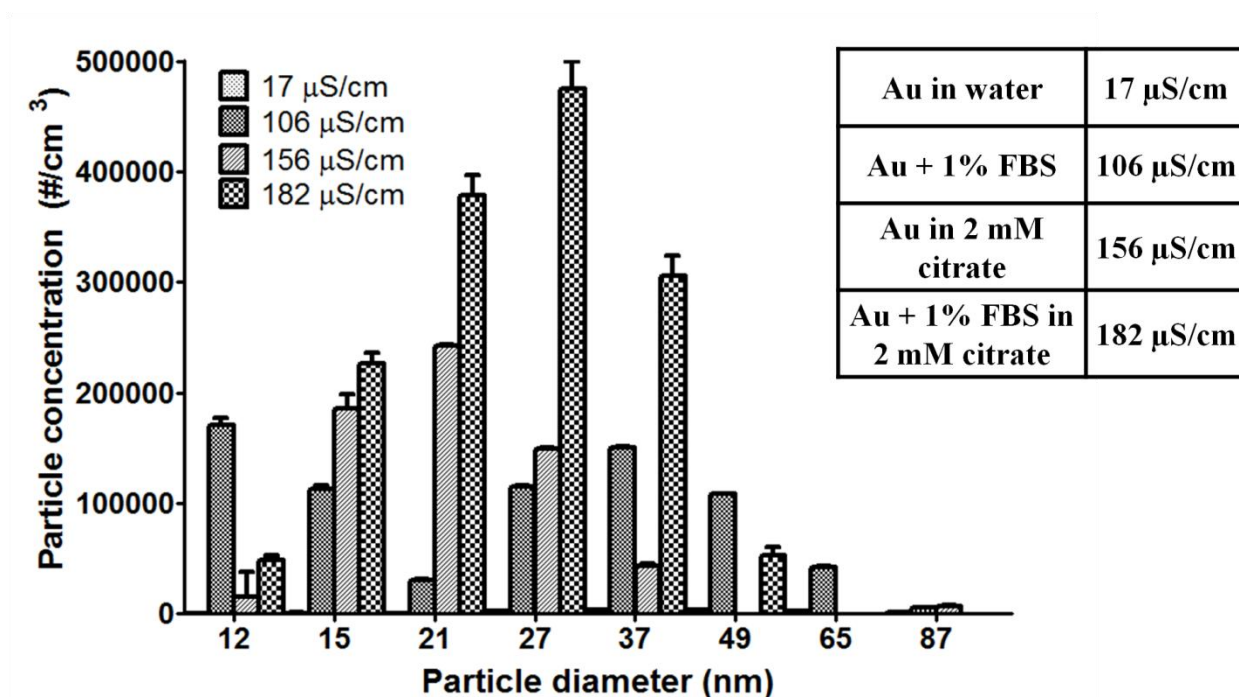


Figure 13. Number size distribution of aerosolized 10 nm Au NMs as a function of conductivity using the Nanoscan SMPS from TSI.

The deposition was carried out with AC electric field strength of 15 kV/cm and frequency of 0.65 or 1.6 Hz (figure 14). The particles were deposited as singlets. Based on the images, it is difficult to determine a quantitative difference between the 2 frequencies. Therefore, the next phase of the project was to try to quantify the deposition.

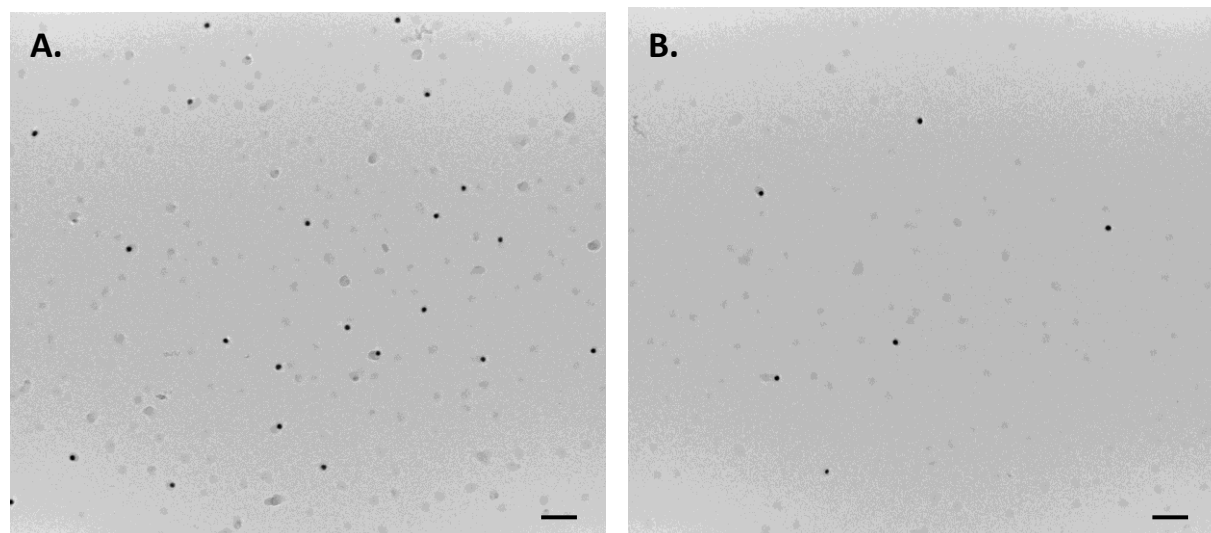


Figure 14. Deposition of gold nanoparticles aerosolized by electrospray with settings: 15 kV/cm and A. 0.65 Hz; B. 1.6 Hz. The scale bar is equal to 100 nm.

DISTRIBUTION A: Approved for public release; distribution unlimited, PA# 88ABW-2013-4142

For quantitative experiments, the nanoparticles were deposited using settings of 15 kV/cm and 0.65 Hz. Substrates investigated included wetted and non-wetted microcellulose ester filters and collagen coated and uncoated glass coverslips. The experiments were repeated 9 times. The substrates were transferred to 15 mL conical tubes. The microcellulose membrane filters and gold particles were dissolved using hydrochloric acid and nitric acid at a ratio of 1:3. The glass coverslips were left in the tubes and pushed to the bottom to be sure they did not interfere with the measurements. The samples were analyzed using inductively coupled plasma – mass spectrometry (ICP-MS). There was no quantifiable deposition.

A schematic of the relative size of the copper grids used for TEM imaging *versus* the glass coverslips used for ICP-MS quantification *versus* the total cell growth area is shown in figure 15. In order to determine if it is feasible for there to be no deposition, some calculations were performed. First, the average number of particles imaged on the copper grids in TEM was determined by counting particles/image and adjusting for the surface area of the grid. Next the average number of particles/glass coverslip was calculated by adjusting for the surface area of a coverslip. This was converted to mass, and the concentration based on the volume of acids used for digestion was calculated. This was also repeated for the cell layer (Table 1). The expected concentration in mass based on particle numbers in TEM images was found to be below the detection limit of ICP-MS. Therefore, longer deposition times must be used or additional techniques must be realized to reach detectable concentrations.

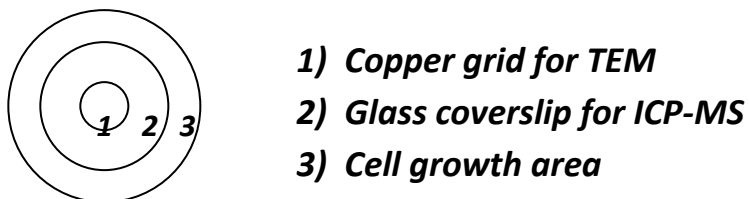


Figure 15. Schematic of the relative size of the copper grids used for TEM versus the glass coverslips used for ICP-MS quantification versus the total cell growth area

Table 1. Expected Deposited Concentration

PARAMETER	VALUE	UNITS
Average number of particles/surface area	2.60E-06	#/nm ²
Surface area of a TEM grid	7.31E+12	nm ²
Number of particles per grid	1.90E+07	particles/grid
Surface area of a glass coverslip	5.03E-01	cm ²
Number of particles per coverslip	1.31E+08	particles/coverslip
Surface area of the insert for cell growth	1.12E+00	cm ²
Number of particles per area for cells	2.91E+08	particles/insert
Mass of Au per coverslip	2.90E-03	µg
Mass of Au per cell insert	6.47E-03	µg
Volume of acids used to digest the particles	0.005	L
Concentration estimated a glass coverslip	5.81E-01	µg/L
Concentration estimated on cell growth area	1.29E+00	µg/L
Lower limit of the ICP-MS	3	µg/L

There were challenges verifying the effect of small changes in frequency on deposition experimentally, due to limited techniques available to quantify the deposition of 10 nm particles. TEM does not include a large enough sample size to be quantitative. Scanning electron microscopy requires sputter coating for low levels of deposition, which is typically gold, so it is difficult to quantify the Au NMs deposited by electrospray in the chamber *versus* the sputter coating. Mass spectrometry has lower detection limits that are too high to detect deposition of NMs that represent realistic *in vivo* conditions (determined using the Multiple Path Particle Dosimetry model). Also, 10 nm NMs cannot be imaged optically. Further research is being conducted to either functionalize the NMs with a fluorophore or to work with slightly larger particles that can be quantified using hyperspectral imaging (lower limit \cong 20 nm).

In order to determine whether the concentration calculated in Table 1 for deposition on the cell layer is relevant for realistic exposure levels, the deposition in the respiratory tract for gold nanoparticles (10 nm) was estimated using the Multiple Path Particle Deposition (MPPD) model. The initial aerosol concentration was set to 0.1 mg/m³, and the deposition was plotted for 1 breath as a function of generation number (figure 16).

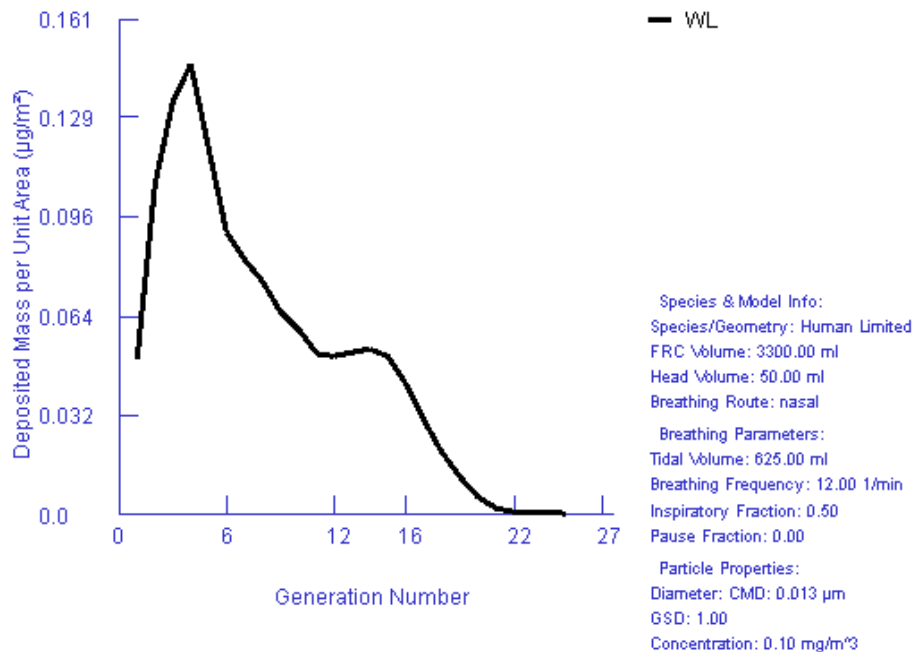


Figure 16. Theoretical deposition of 10 nm gold nanoparticles in the respiratory tract as a function of generation number for 1 breath, estimated using the MPPD model.

Next, the deposition was calculated for a 1 hour exposure for direct comparison to the values displayed in Table 1. For this calculation, it was assumed that a human takes 12 breaths per minute. The calculation was completed using equation 11 for both peaks shown in figure 17.

$$M_{dep} \left[\frac{\mu g}{cm^2} \right] = \frac{MPPD \left[\frac{\mu g}{m^2 * breath} \right] * 12 \left[\frac{breath}{min} \right]}{t[min] * 100^2 \left[\frac{cm^2}{m^2} \right]} \quad (11)$$

The results for this calculation are shown in Table 2 and compared with the deposited mass estimated from the TEM grids. The results of this comparison demonstrates that although the mass deposited on the coverslips after 1 hour were not detected using ICP-MS, they are still relevant.

Table 2. Mass Deposition Calculated using the MPPD Model

PARAMETER	VALUE	UNITS
Exposure limit (used for Ag) ¹	0.1	mg/m ³
MPPD output (µg/m ² deposited per breath) peak 1	0.13	µg/m ²
MPPD output (µg/m ² deposited per breath) peak 2	0.05	µg/m ²
M _{dep} peak 1	9.36E-03	µg/cm ²
M _{dep} peak 2	3.60E-03	µg/cm ²
Total mass of Au per cell insert	5.78E-03	µg/cm²

Longer exposure times will be used in future experiments for generating quantifiable nanoparticle deposition. The minimum exposure time based on the calculations shown here is expected to be 8 hours.

A poster was presented on the NM aerosol dosimetry described in previous reports at the annual Society of Toxicology meeting on 12 March 2013 by Ms. Christin Grabinski (figure 17). Based on the quality of the poster abstract and reference letters, Ms. Grabinski was awarded First Place, Outstanding Graduate Student, sponsored by the Nanotoxicology Specialty Section of the Society of Toxicology.



Realistic Assessment of NM Toxicity *In Vitro* using a Nanoaerosol Exposure Chamber

Christin Grabinski^{1,2}, Mohan Sankaran², and Saber M. Hussain¹

¹711 HPW/RHDJ, Air Force Research Laboratory, Wright-Patterson AFB, OH

²Department of Chemical Engineering, Case Western Reserve University, Cleveland, OH



Background

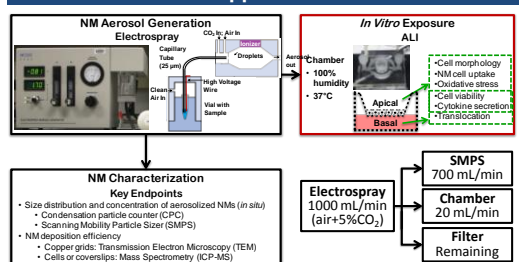
Nanomaterials (NMs) are being implemented in many Air Force applications, such as fuels, weapons, and sensors. Inhalation is the key route of concern for occupational exposure to NMs.

Traditional *in vitro* toxicity assays require that NMs are dispersed in biological media prior to exposure, which can alter their properties and affect dosimetry (Grabinski et al.; 2011; Hussain et al., 2009; Cho et al., 2011). Therefore, it is critical to develop methods for exposing cells to aerosolized NMs at the air-liquid interface (ALI).

Objective

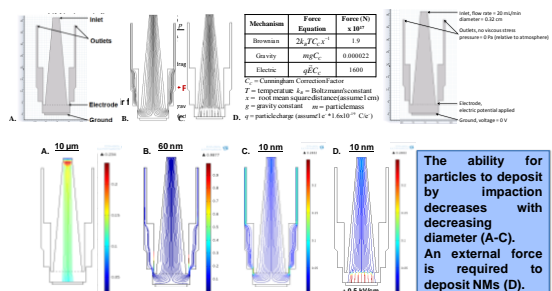
The objective is to develop the instrumentation and methodology for exposing aerosolized NMs to substrates at the ALI. Specifically, we aim to control the deposition of NMs by adjusting the electric field properties to achieve realistic doses for inhalation exposure

Approach



Theory

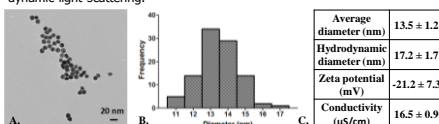
In order to understand the deposition of NMs in the chamber, the particle trajectories were modeled using multi-physics software (Comsol 4.2a).



Results

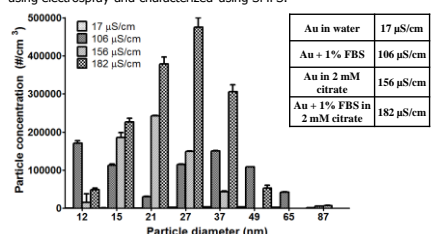
NM Characterization

Gold NMs were characterized in their as-synthesized form using TEM and dynamic light scattering.



Characterization of gold NMs. A. Electron micrograph; B. Histogram of the size distribution; C. Table with data for average diameter, hydrodynamic diameter, zeta potential and conductivity.

Gold NMs were diluted in water or 2 mM citrate to 100 µg/mL, aerosolized using electro spray and characterized using SMPS.



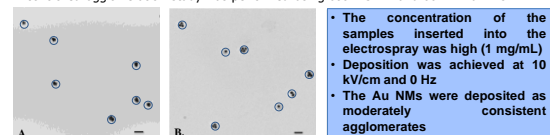
Data show that aerosol concentration increased with increasing conductivity

Total aerosol concentration in order of increasing conductivity: 1.4 x 10⁴ #/cm³; 7.3 x 10⁵ #/cm³; 1.1 x 10⁶ #/cm³; 1.6 x 10⁶ #/cm³

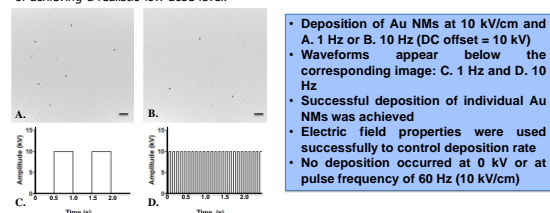
NM Aerosolization and Deposition

The NM aerosols were passed through a bipolar charger at the exit of the electro spray. The charged NM aerosols were drawn into the nanoaerosol chamber at a flow rate of 20 mL/min. The NMs were deposited for 1 hour onto copper grids by applying an electric field in the chamber. The deposition was characterized using TEM (scale bars = 100 nm).

A controlled agglomeration study was performed using both 13 nm and 60 nm Au NMs.



The effect of electric field pulse frequency was investigated using 13 nm Au NMs with the goal of achieving a realistic low dose level.



Semi-quantitative calculations were conducted for Au NM deposition with a pulsed frequency of 1 and 10 Hz shown above. The number of particles per micrograph surface area was averaged at each frequency. The results were found to be: 2.7 x 10⁸ particles/cm² at 1 Hz and 4.5 x 10⁷ particles/cm² at 10 Hz.

Relevance

The Multiple Path Particle Dosimetry Model (MPPD) was used to predict a realistic dose for inhalation exposure of Au NMs. The model is based on published theoretical efficiencies for particle deposition (Anjilvel, 1995).

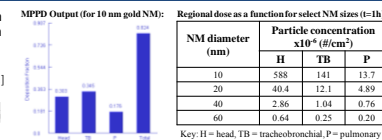
Deposited number concentration ($N_{dep}(t)$) = $N_{aero}(t) \left[\frac{particles}{cm^3} \right] = MPPD \left[\frac{particles}{cm^3 \cdot breath} \right] \cdot \left[\frac{breath}{min} \right] \cdot t$ [min]

where t = exposure time

Deposited number concentration ($M_{dep}(t)$) = $N_{aero}(t) \left[\frac{particles}{cm^3} \right] \cdot \left[\frac{m^2}{6 \cdot particle} \right] \cdot \left[\frac{g}{cm^3} \right] \cdot \left[\frac{g}{cm^3} \right]$

where d_p = particle diameter

ρ_p = particle density



Conclusion and Future Work

The results of this study demonstrate that electric field properties can be varied as a realistic approach for dosing aerosolized NMs for *in vitro* inhalation toxicity assessment. Future work will be performed to systematically investigate the toxicity of Au and Ag NMs at the air-liquid interface.

Acknowledgements

This work is funded by the Office of the Air Force Surgeon General. Ms. Grabinski receives a fellowship from the Oak Ridge Institute for Science and Education. We thank Dr. Hari Baskaran (Case Western Reserve University) for his help obtaining access to Comsol multi-physics software.

References

Hussain et al. *Adv. Mater.* **2009**, *21*, 1549–59.
Grabinski et al. *ACS Nano* **2011**, *5*, 2870–9.
Anjilvel and Asgharian. *Fundam. Appl. Toxicol.* **1995**, *28*, 41–50.
Cho et al. *Nature Nanotechnol.* **2011**, *6*, 385.

Distribution A. Approved for public release; distribution unlimited. Clearance number: 88ABW-2013-0394.

Figure 17. Poster presented at the Society of Toxicology Annual Meeting in San Antonio, TX on 12 March 2013.

In order to allow for air-liquid interface toxicity investigations using a broader range of Air Force relevant NMs, we investigated additional approaches for NM aerosolization. Approaches for NM aerosolization can be categorized into three categories: (1) synthesize in gas phase, (2) aerosolize from a liquid, and (3) aerosolize from a powder. These approaches are described in further detail in Table 3.

Table 3. Summary of Key Approaches Available for NM Aerosolization

Approach	Method	Advantages	Disadvantages
Synthesize NM aerosols in gas phase	e.g. microplasma	Reproducible; can be used to generate monodisperse NM aerosols	Limited to very specific NMs, which may not exist in an operational environment
Aerosolize NMs from a liquid dispersion	electrospray	Reproducible; can be used to generate monodisperse NM aerosols	Limited to NMs that can be dispersed in a conductive buffer
	nebulizer	Common in medical industry	Many AF relevant NMs cannot be dispersed in an aqueous media; aerosols are polydisperse
Aerosolize NMs from a powder	powder aerosolizer	Eliminates requirement to disperse nanopowders in an aqueous media; can be used to produce aerosols for many AF relevant NMs	Limited to NMs, which are synthesized as a powder or can be dried in large quantities (≥ 100 mg); aerosols are polydisperse

Powder aerosolization was chosen as an approach that will allow for a broader range of Air Force relevant NMs to be aerosolized. Many approaches for aerosolizing nanopowders were investigated, including brush generators, belt generators, and jet mills. However, these instruments are appropriate for greater scale studies than we need, requiring a large amount of space and powder. There were two instruments identified as relevant to fit our needs. These include the Small Scale Powder Disperser (SSPD; TSI) and the Vilnius Aerosol Generator (VAG; CH Technologies). The SSPD operates using a Venturi throat aspirator (figure 18A), and the VAG operates using a series of jets and an oscillating turbine (figure 18B). The VAG incorporates a feedback control to ensure constant aerosol generation.

DISTRIBUTION A: Approved for public release; distribution unlimited, PA# 88ABW-2013-4142

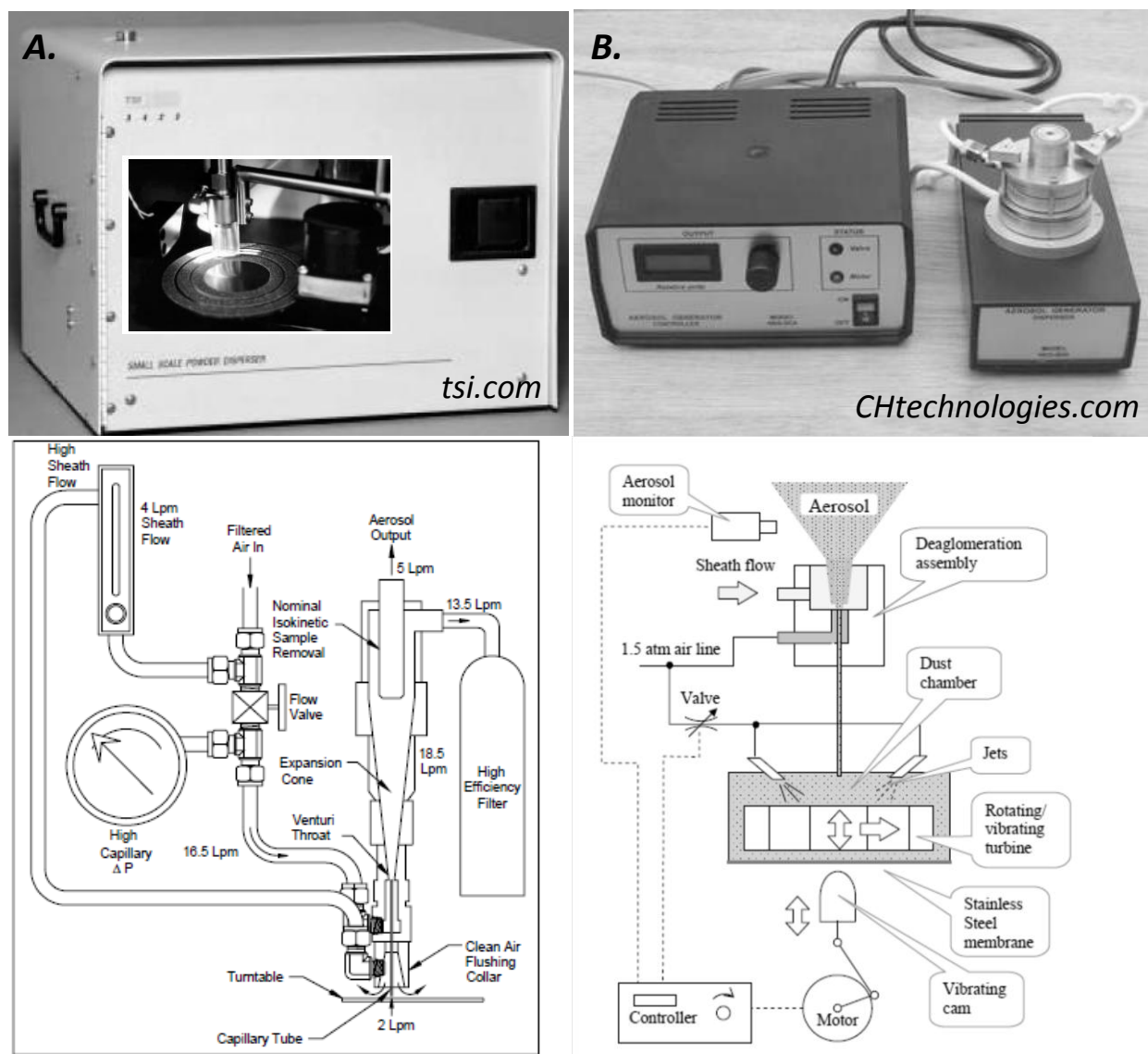


Figure 18. Image and operation schematics for dry powder aerosol generation instruments. A. SSPD; B. VAG.

To compare the SSPD and the VAG, aluminum nanopowder (~50 nm) was aerosolized and characterized for size distribution using a Scanning Mobility Particle Sizer (SMPS, TSI) and deposition using a Nanomaterial Aerosol Sampler (TSI) and electron microscopy. We do not have access to an SMPS in our laboratory, so we used instruments at Case Western Reserve University (CWRU) and in the Navy laboratory. The results are shown in Table 4. The data are a result of three scans each lasting 120 seconds.

Table 4. SMPS Data for the SSPD and VAG

Endpoint	SSPD (CWRU SMPS)		VAG (NAVY SMPS)	
	Average	St. Dev.	Average	St. Dev.
Particle concentration (#/cm ³)	1.9 x10 ⁴	1.6 x10 ⁴	2.1x10 ⁴	1.5x10 ³
Mass Median Diameter (nm)	53.9	6.4	155	4.8

The SMPS data indicated a larger variability for particle concentration using the SSPD. This is due to the fact that it is difficult to introduce a consistent amount of powder on the turntable. After initiating experiments, it was realized that the mass median diameter data were not comparable. The SMPS at CWRU is calibrated to measure small NMs, so the upper limit is 60 nm. The upper limit for the Navy SMPS is close to 1000 nm, so this data is more reliable. Regardless, based on this data and discussion with various experts in the aerosol field, it was determined that the VAG was the most appropriate instrument for our studies.

For size, the Al NMs were deposited on TEM grids using an electrostatic precipitator set to -10 kV. The results are shown in figure 19. The data show that large agglomerates were deposited (> 100 nm). To produce more uniform deposition, we propose to use only stainless steel and conductive silicone tubing for transport (Navy set-up used some plastic tubing). Also, applying a controlled uniform charge on the aerosols is expected to reduce agglomeration.

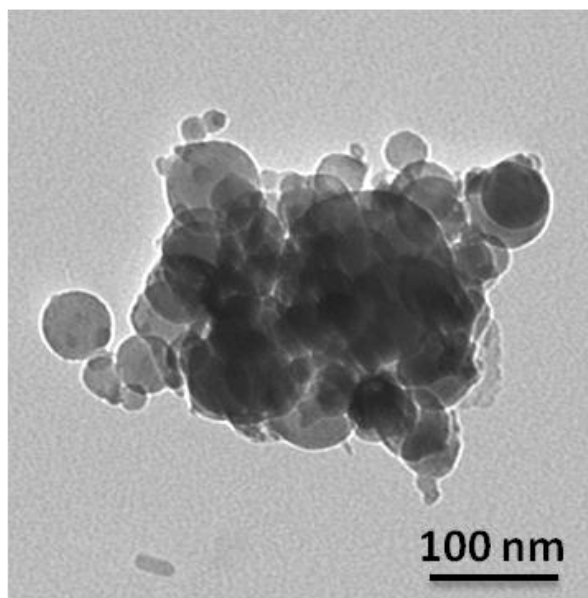
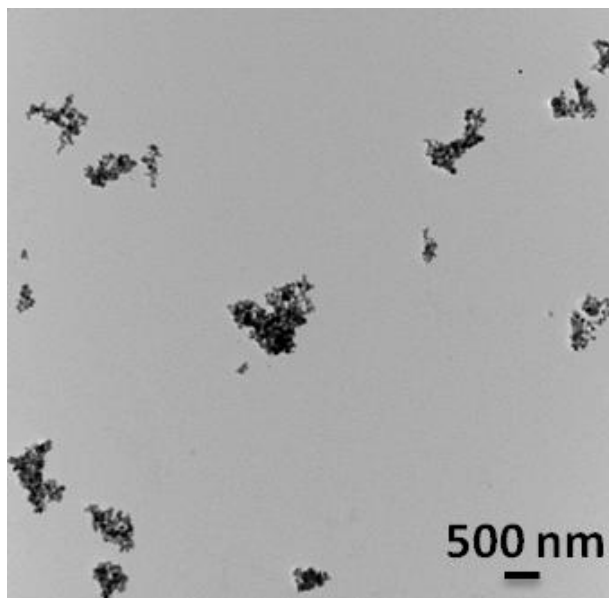


Figure 19. Al NMs aerosolized using the VAG and deposited onto TEM grids using electrostatic precipitation.

The instrumentation acquired for NM powder aerosolization and characterization are shown in Figure 20.

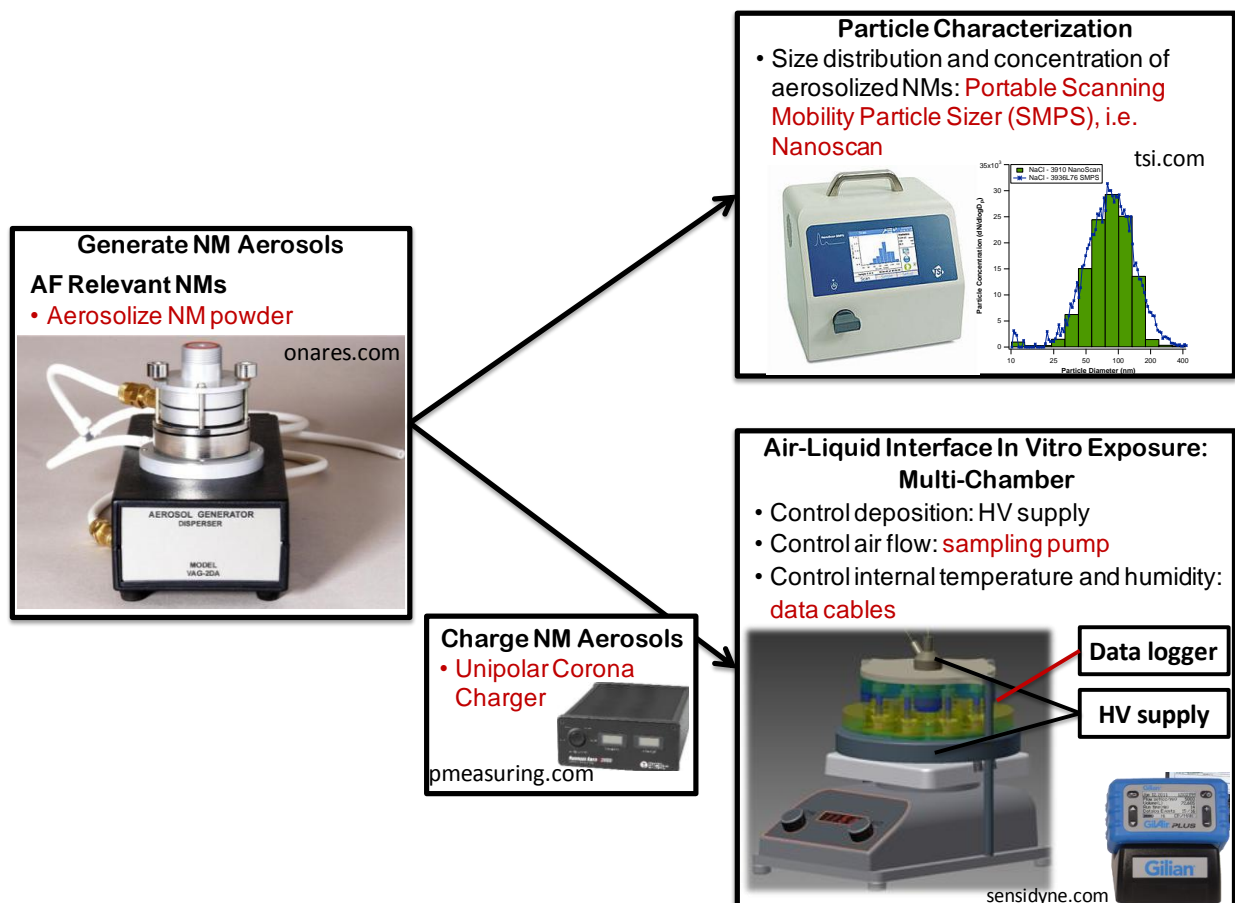


Figure 20. Schematic for NM aerosol exposure using a powder aerosolization method. The new additions are shown in red.

A list of the instruments and materials purchased is shown in Table 5. The first three items will be purchased in November due to in-house paperwork processing time. The rest of the items were purchased and acquired in October 2012.

Table 5. Specific Instrument Requirements for NM Aerosolization and Characterization

Item	Description	Justification	Cost
Vilnius Aerosol Generator	Produces nano-sized aerosols from powder	Required for hydrophobic materials, which do not disperse in aqueous media	\$20,360
NanoScan, Scanning Mobility Particle Sizer (SMPS)	Portable SMPS; measures size distribution of NM aerosols	Required for in situ characterization of NM aerosols	\$29,900
Unipolar corona charger	Charges NM aerosols	Required for electrostatic deposition	\$8,450
GilAir Plus STP Single Starter Kit	Accurate low flow rate, high accuracy vacuum pump	Required to control air flow into the chamber	\$1140
Gilian Gilibrator-2 Calibrator Kit	Calibrator for the sampling pump	Required to calibrate the pump	\$1,695
Gilibrator SmartCal Calibrator Cable	Cable to allow continuous calibration of the sampling pump	Required for continuous calibration to account for variation in pressure drop	\$94
Conductive silicone tubing	Transports aerosols	Required for delivering NM aerosols with minimal tubing loss	\$367
Capillaries for electrospray	Draw NMs from liquid dispersion to aerosol	Required consumable for the electrospray	\$675
Data cable assembly	Set of cables to connect humidity sensor to data logger	Required for real-time monitoring of humidity inside the chamber	\$2,900
316 Stainless steel tubing	Transports aerosols	Required for delivering NM aerosols with minimal tubing loss	\$57

Metal tubing cutter	Cuts 316 SS tubing to desired length	Required for NM aerosol transport	\$46
Total			\$65,683

The key components of the project include (1) developing a chamber for exposing *in vitro* models to aerosolized NMs, (2) investigating the dosimetry of aerosolized NMs in the chamber and (3) investigating toxicity endpoints. In order to address the first point, a scaled-up multi-chamber was designed. A schematic of the scaled up chamber is shown in figure 21.

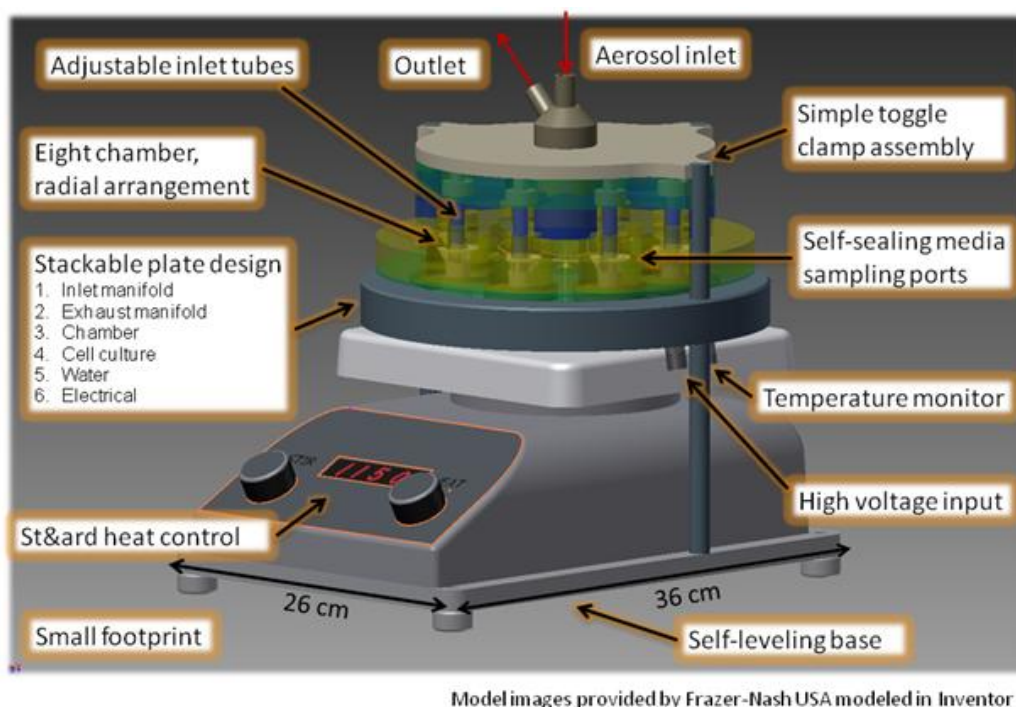


Figure 21. Multi-chamber model

Preliminary cell-based experiments were conducted using the scaled-up multi-chamber. For this, type II pneumocytes (A549 cells) were used. The cells were seeded at 5×10^4 cells/cm² on 0.4 micron pore polyester membrane inserts (Transwells™, Corning). The cells were fed fresh media after 2 days, then the apical media was removed on the 3rd day, and the cells were allowed to polarize at the air-liquid interface overnight. On the 4th day, the membrane inserts were transferred to the chamber and exposed to mixed air (95% air + 5% carbon dioxide) for 1 hour at 80 mL/min (10 mL/min / membrane insert) with or without an electric field (5 kV/cm, 0.2 Hz).

The air humidity and temperature within the chamber was measured using analog humidity/temperature sensors (Sensirion) located near the cell layer for each membrane insert (8 total, arranged radially). The signal from the sensors was monitored using an analog to digital converter and data logger. The electric field in the chamber was generated using a function generator and amplifier for the high voltage input and grounding the water bath beneath the chambers. A picture of the portable chamber is shown in figure 22.

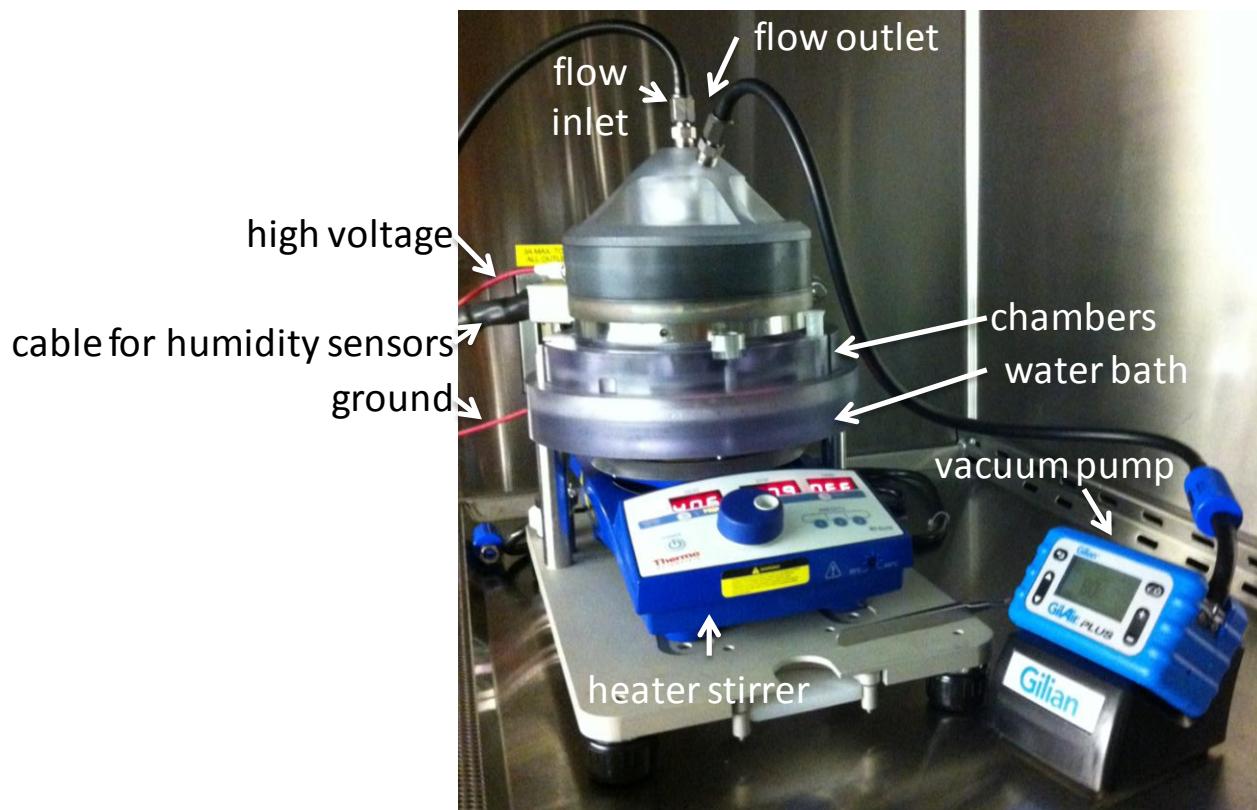


Figure 22. Picture of the portable chamber set-up.

The relative humidity and temperature in the chamber was maintained at $68.68 \pm 1.42\%$, and $27.18 \pm 0.05^\circ\text{C}$, respectively (figure 23). It is expected that maintaining the humidity and temperature close to incubator conditions (100% humidity, 37°C) will maximize the length of time the cells can be sustained in the chamber. The relative humidity within the chamber is controlled by two mechanisms. The first is the water bath, where water is wicked through the central column of the chamber into the air stream using a passive mechanism, and the second is evaporation of the cell media. After the 1 hour exposure, about $50\ \mu\text{L}$ of media evaporated. The membrane inserts were still submerged under this condition. However, for longer exposures, the media may need to be replenished.



Figure 23. Output screens on the humidity data logger used to collect data from the humidity/temperature sensors within the chamber.

The viability was assessed using the Alamar Blue assay, and the cell layers were imaged using light microscopy. The results for the viability assay are shown in figure 24. There was no statistically significant difference from the incubator control (statistical significance determined using a Student's t-test, $p < 0.05$).

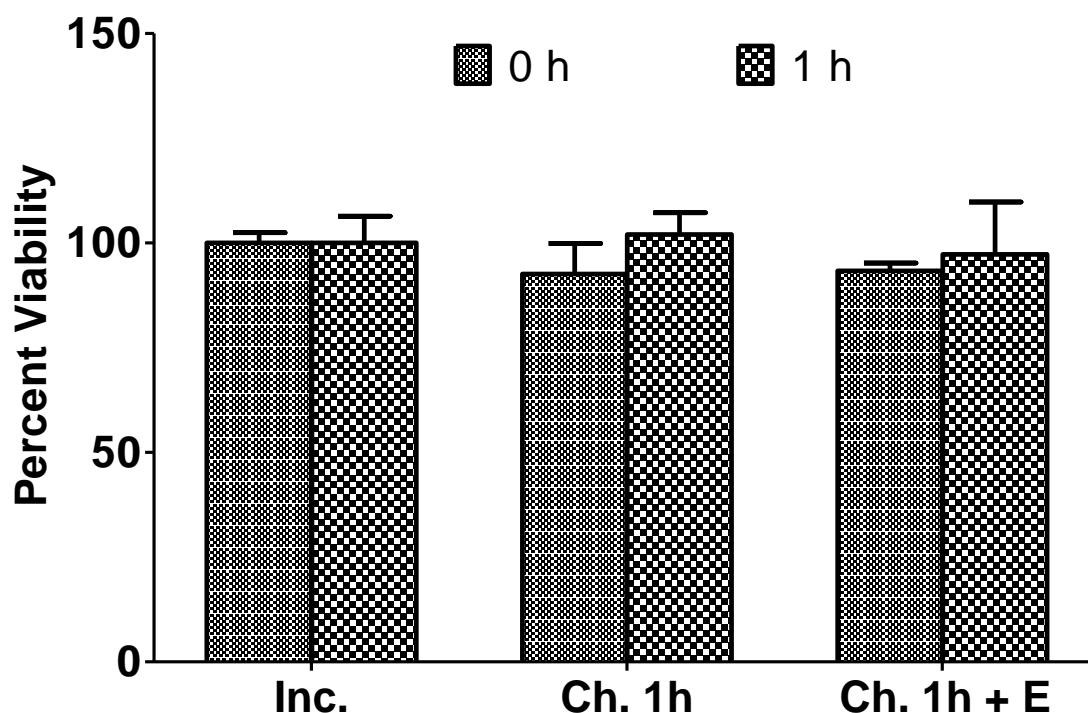


Figure 24. Alamar Blue assay. Inc.=Incubator; Ch.=Chamber; E=Electric field.

In conclusion, we have successfully demonstrated that we developed a realistic nanoaerosol exposure system that can be used to deposit NMs onto cells maintained at the air-liquid interface within a portable chamber for the investigation of NM toxicity. Future work will involve the routine investigation of NM toxicity using this system and

correlation with traditional exposures, in addition to published or concurrent *in vivo* results.

References

[1] Li and Ahmadi (2012). Aerosol Sci Technol. 16: 209.

[2] Savi et al. (2008) Environ. Sci. Technol. 42: 5667

B. Evaluate chamber generated nanomaterials *continued*

- *Establish a fundamental mechanism of interaction of NMs with biological molecules and develop kinetic models to predict toxicity or biocompatibility*

This bullet is being addressed through interaction with collaborators, specifically with Dr. Ravindra Pandey at the Michigan Technological University and Dr. Jerzy Leszczynski at Jackson State University. The first modeling approach was molecular dynamics to understand interactions between nanoparticles and lipid membranes conducted in collaboration with Dr. Ravindra Pandey, Michigan Technological University, Houghton, MI. An extensive report describing this work was submitted in the Phase II final report. The second modeling approach was on quantitative structure activity relationships (QSARs). A manuscript entitled “Connecting the dots: Towards understanding complexity of the mechanisms of nanoparticles cytotoxicity” was submitted to PNAS and is paraphrased below:

The production of NMs increases every year exponentially and therefore the probability that they could cause adverse outcomes for human health and the environment also expands rapidly. We proposed two types of mechanisms of toxic action supported by the nano-QSAR model, which collectively govern the toxicity of the metal oxide nanoparticles to the human keratinocyte cell line (HaCaT). The combined experimental-theoretical study allowed us to develop an interpretative nano-QSAR model describing toxicity of 18 nano-metal oxides to a HaCaT cell line as a model for dermal exposure. In result, by the comparison of the toxicity of metal oxide nanoparticles to bacteria *Escherichia coli* (prokaryotic system) and a human keratinocyte cell line (eukaryotic system), we hypothesized different modes of toxic action occur between prokaryotic and eukaryotic systems. Various products of nanotechnology are utilized in numerous areas of human life: in commercial products, medicine, cosmetics, etc.

One of the basic principles of QSAR modeling is finding structural parameters (descriptors) that are responsible for the property of interest, i.e. toxicity. The descriptors, which are important in understanding the peculiar effects of NMs, include particle size and size distribution, agglomeration state, particle shape, crystal structure, chemical composition, surface area, surface chemistry, surface charge, electronic

properties (reactivity, conductivity, interaction energies, etc.), and porosity (11-14). The descriptors can be either derived from experimental data or calculated with various theoretical approaches (i.e., quantum chemistry). Recently (15), we have developed a nano-QSAR model employing a theoretical, quantum-chemical descriptor which was able to successfully predict the *in vitro* toxicity on *E. coli* bacteria for a series of metal oxide nanoparticles. This model (eq. 12) contains only one descriptor, ΔH_{Me+} , which represents the enthalpy of formation of a gaseous cation having the same oxidation state as that in the metal oxide structure:

$$\log (EC_{50})^{-1} = 2.59 - 0.50 \Delta H_{Me+} \quad (12)$$

Here, we have expanded nano-QSAR model to describe a mammalian system. This allows elucidating the relationship between the structure and toxicity of 18 nano-metal oxides to HaCaT cell line considered as a model for dermal exposure. The present study was aimed at exposing and explaining differences in modes of toxic action of metal oxide nanoparticles between the eukaryotic system (HaCaT) and the prokaryotic system (*E. coli*).

Simultaneously to the experimental toxicity testing, we calculated a set of 27 parameters quantitatively describing variability of the nanoparticles' structure - nano-descriptors (Table 6). These included: 16 quantum-mechanical descriptors (from quantum-chemical calculations) and 11 image descriptors (derived from TEM images).

Table 6. Symbols and Definitions of All Calculated Molecular Descriptors

Symbol	Definition of molecular descriptor	Included?
QUANTUM - MECHANICAL DESCRIPTORS		
ΔH_f^c	Standard enthalpy of formation of metal oxide nanocluster	Yes
TE	Total energy	No
EE	Electronic energy	No
Core	Core–core repulsion energy	No
SAS	Solvent accessible surface	No
HOMO	Energy of the Highest Occupied Molecular Orbital	No
LUMO	Energy of the Lowest Unoccupied Molecular Orbital	No
E_g	HOMO-LUMO energy gap	No
μ	Electronic chemical potential	No
E_v	Valance band	No
E_c	Conduction band	No
χ^c	Mulliken's electronegativity	Yes
Hard	Parr and Pople's absolute hardness	No
Shift	Schuurmann MO shift alpha	No
Ahof	Polarizability derived from the heat of formation	No
Ad	Polarizability derived from the dipole moment	No
IMAGE DESCRIPTORS		
A	Area	No
V	Volume	No
d_s	Surface diameter	No
$d_{V/m}$	Volume/mass diameter	No
d_{Sauter}	Volume/surface diameter	No
A_{R_x}	Aspect ratio X	No
A_{R_y}	Aspect ratio Y	No
P_x	Porosity X	No
P_y	Porosity Y	No
Ψ	Sphericity	No
f_{circ}	Circularity	No

Since from the quantum-chemical point of view even a nanoparticle of about 15 nm is too large of a system to perform accurate calculations, it was necessary to maximally simplify the structural model. Indeed, we calculated selected electronic properties based on small, stoichiometric clusters, reflecting all characteristics of fragments of crystal structures (surface) of particular oxides. All the clusters were of the same size: $0.5 \times 0.5 \times 0.5$ nm. A complete list of the crystallographic data (bond lengths, valence and torsion angles) used for constructing the clusters is described in Table 7. The quantum–mechanical calculations included two steps: (i) optimization of the molecular geometry with respect to the energy gradient and (ii) calculation of the descriptors based on the optimized geometry. The descriptors reflect electronic properties of the surface.

Table 7. Crystallographic Data Utilized to Construct Metal Oxide Clusters

Metal oxide	Reference
Al ₂ O ₃	Kondo, S., Tateishi K., Ishizawa N., <i>Structural Evolution of Corundum at High Temperatures</i> . Japanese Journal of Applied Physics, 2008. 47 : p. 616-619
Bi ₂ O ₃	Cornei, N., Tancret N., Abraham F., Mentré O., New epsilon-Bi ₂ O ₃ metastable polymorph. Inorganic Chemistry, 2006. 26 : p. 4886-4888.
CoO	Saito, S., Nakahigashi K., Shimomura Y., X-Ray Diffraction Study on CoO. Journal of the Physical Society of Japan, 1966. 21 : p. 850-860.
Cr ₂ O ₃	Finger, L.W., Hazen R.M., Crystal structure and isothermal compression of Fe ₂ O ₃ , Cr ₂ O ₃ , and V ₂ O ₃ to 50 kbars Journal of Applied Physics, 1980. 51 : p. 5362-5368
Fe ₂ O ₃	Hill, A.H., Jiao F., Bruce P.G., Harrison A., Kockelmann W., Ritter C., Neutron Diffraction Study of Mesoporous and Bulk Hematite, α -Fe ₂ O ₃ . Chemistry of Materials, 2008. 20 : p. 4891–4899.
In ₂ O ₃	Prewitt, C.T., Shannon R.D., Rogers D.B., The C Rare Earth Oxide-Corundum Transition and Crystal Chemistry of Oxides Having the Corundum Structure. Inorganic Chemistry, 1969. 8 : p. 1985-1993.
La ₂ O ₃	Wu, B., Zinkevich M., Aldinger F., Wen D., Chen L., Ab initio study on structure and phase transition of A- and B-type rare-earth sesquioxides Ln ₂ O ₃ (Ln=La–Lu, Y, and Sc) based on density function theory. Journal of Solid State Chemistry, 2007. 180 : p. 3280-3287.
Mn ₂ O ₃	Norrestam, R., Ingri N., Östlund E., Bloom G., Hagen G., alpha-Manganese(III) Oxide --- a C-Type Sesquioxide of Orthorhombic Symmetry Acta Chemica Scandinavica, 1967. 21 : p. 2871-2884.
NiO	Shimomura, Y., Kojima M., Saito S., Crystal structure of ferromagnetic nickel oxide. Journal of the Physical Society of Japan, 1956. 11 : p. 1136-1146.
Sb ₂ O ₃	Whitten, A.E., Dittrich B., Spackman M.A., Turner P., Brown T.C., Charge density analysis of two polymorphs of antimony(III) oxide. Dalton Transactions, 2004. 7 : p. 23-29.
SiO ₂	Martinez, J.R., Palomares-Sanchez S., Ortega-Zarzosa G., Ruiz F., Chumakov Y., Rietveld refinement of amorphous SiO ₂ prepared via sol–gel method. Materials Letters, 2006. 60 : p. 3526–3529.
SnO ₂	Gracia, L., Beltrán A., Andrés J., Characterization of the high-pressure structures and phase transformations in SnO ₂ . A density functional theory study. The Journal of Physical Chemistry B, 2007. 111 : p. 6479-6485.
TiO ₂	Swamy, V., Dubrovinsky L.S., Dubrovinskaia N.A., Langenhorst F., Simionovici A.S., Drakopoulos M., Dmitriev V., Weber H.P., Size effects on the structure and phase transition behavior of baddeleyite TiO ₂ . Solid State Communications, 2005. 134 : p. 541–546.
V ₂ O ₃	Rozier, P., Ratuszna A., Galy J., Comparative structural and electrical studies of V ₂ O ₃ and V ₂ -xNixO ₃ (0<x<0.75) solid solution. Zeitschrift für Anorganische und Allgemeine Chemie, 2002. 628 : p. 1236-1242.
WO ₃	Woodward, P.M., Sleight A.W., Vogt T., Ferroelectric Tungsten Trioxide Journal of Solid State Chemistry, 1997. 131 : p. 9-17.
Y ₂ O ₃	Santos, C., Strecker K., Suzuki P.A., Kycia S., Silva O.M.M., Silva C., Stabilization of alpha-SIALONS using a rare-earth mixed oxide (RE ₂ O ₃) as sintering additive. Materials Research Bulletin, 2005. 40 : p. 1094-1103.
ZnO	Singhal, R.K., Samariya A., Xing Y.-T., Kumar S., Dolia S.N., Deshpande U.P., Shripathi T., Saitovitch E.B., <i>Electronic and magnetic properties of Co-doped Zn O diluted magnetic semiconductor</i> . The Journal of Alloys and Compounds, 2010. 496 : p. 324-330.
ZrO ₂	Naray-Szabo, S., <i>Zur Struktur des Baddeleyits ZrO₂</i> . Zeitschrift fuer Kristallographie, Kristallgeometrie, Kristallphysik, Kristallchemie, 1936. 94 : p. 414-416.

The TEM microscopic images obtained at the stage of experimental characterization of the nanoparticles were utilized for calculating a set of image descriptors that reflect the size, size distribution, shape, porosity, and surface area for all studied nanometer–sized metal and semimetal oxides.

Based on the toxicity data and carefully selected structural descriptors (Table 8), we developed a nano-QSAR model, employing a hybrid Genetic Algorithm - Multiple Linear Regression as the modeling method.

Table 8. Data on the Structure and Toxicity used in the Study

Metal oxide	ΔH_f^c [kcal/mol]	χ^c [eV]	Observed $\log(1/EC_{50})$ [molar]	Set	Predicted $\log(1/EC_{50})$ [molar]	Residuals	Leverages
TiO ₂	-1492.0	4.91	1.76	T	1.78	-0.02	0.71
Al ₂ O ₃	-600.0	3.44	1.85	V	1.90	-0.05	0.28
ZrO ₂	-638.1	4.95	2.02	T	2.25	-0.23	0.13
Fe ₂ O ₃	-378.5	4.21	2.05	V	2.21	-0.16	0.17
SiO ₂	-618.3	3.81	2.12	T	1.99	0.13	0.23
Y ₂ O ₃	-135.3	3.35	2.21	V	2.14	0.07	0.33
V ₂ O ₃	-139.5	3.24	2.24	T	2.11	0.13	0.35
Cr ₂ O ₃	-235.3	4.36	2.30	V	2.33	-0.03	0.17
Sb ₂ O ₃	-206.7	4.46	2.31	T	2.37	-0.06	0.17
NiO	68.0	4.47	2.49	V	2.52	-0.03	0.29
Bi ₂ O ₃	-148.5	5.34	2.50	T	2.62	-0.12	0.16
WO ₃	-715.4	6.73	2.56	V	2.65	-0.09	0.20
Mn ₂ O ₃	-96.3	5.00	2.64	T	2.56	0.08	0.18
SnO ₂	-266.6	4.57	2.67	V	2.36	0.31	0.15
CoO	-786.8	7.44	2.83	T	2.78	0.05	0.32
La ₂ O ₃	-157.7	6.45	2.87	V	2.88	-0.01	0.20
In ₂ O ₃	-52.1	6.78	2.92	T	3.02	-0.10	0.28
ZnO	-449.4	8.33	3.32	T	3.18	0.14	0.46

The nano-QSAR model utilizes only two descriptors for predicting the cytotoxicity of the metal oxide nanoparticles (eq. 13):

$$\log(EC_{50})^{-1} = 2.466 + 0.244 \Delta H_f^c + 0.394 \chi^c \quad (13)$$

$$F = 44.6, p = 1 \times 10^{-4}, n = 18, R^2 = 0.93, RMSE_C = 0.12, Q^2_{CV} = 0.86,$$

$$RMSE_{CV} = 0.16, Q^2_{Ext} = 0.83, RMSE_P = 0.13$$

where: ΔH_f^c is the enthalpy of formation of metal oxide nanocluster representing fragment of the surface and χ^c - the Mulliken's electronegativity of the cluster.

The model has been comprehensively validated according to the OECD QSAR validation recommendations, because it is expected that only a properly validated model can offer a meaningful mechanistic interpretation (16,17). The details are provided in Figure 25. Solid lines represent the residual threshold (0 ± 3 standard deviation units), and the dashed line represents the critical leverage value (h^*). The visual inspection of the plot of standardized cross-validated residuals *versus* leverage values (Williams plot, Figure 25) confirmed that all training and validation compounds were located inside a

squared area within ± 3 standard deviation units and a leverage threshold $h^* = 0.90$. This means, there were no outlying results for metal oxides nanoparticles in both the structural similarity axis and the toxicity predictions. Thus, comprehensive validation of the model itself and its applicability domain demonstrated high predictive ability of the nano-QSAR for the series of the studied nano-metal oxides.

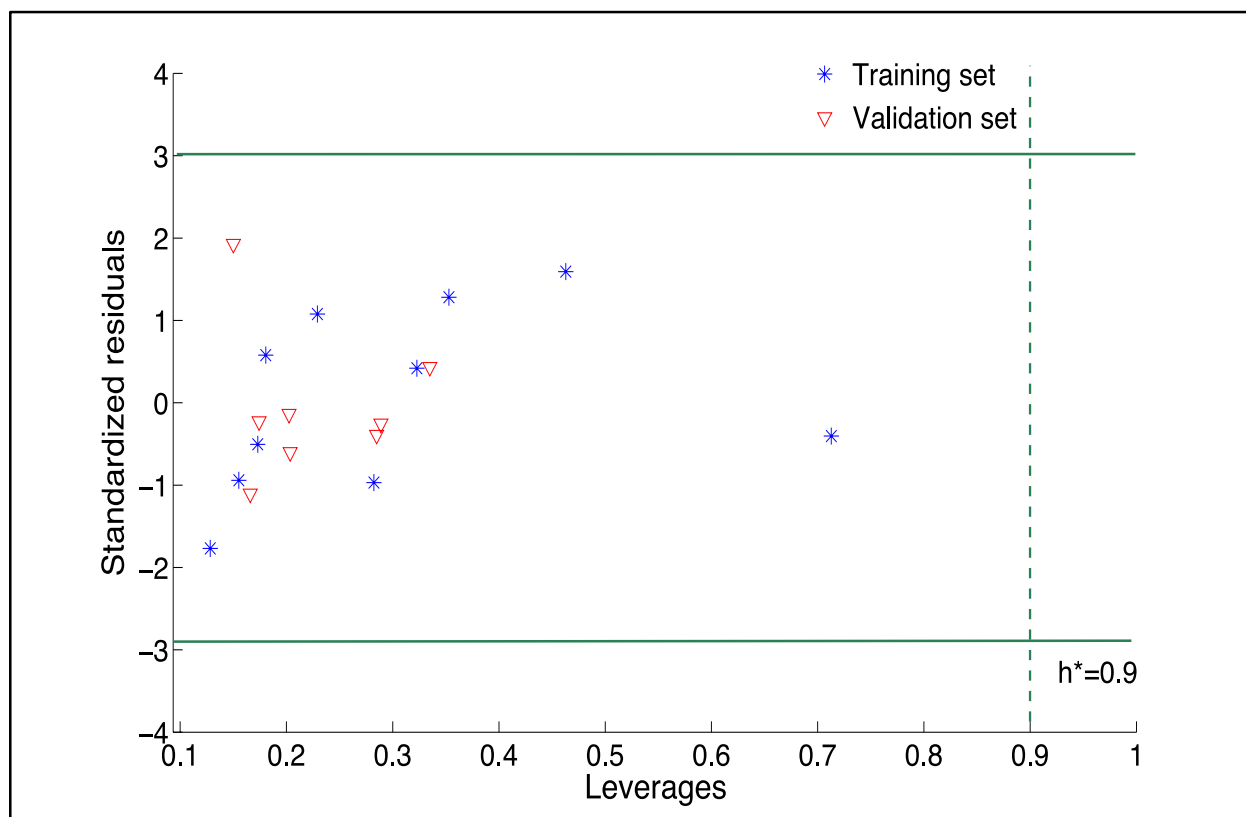


Figure 25. Williams plot describing applicability domains of GA-MLR model

The presented model fulfills all the validation criteria. Moreover, the visual inspection of the plotted relationship between the experimentally determined (observed) and predicted (with nano-QSAR) toxicity of the considered metal oxides (Figure 26) additionally confirms the results of validation.

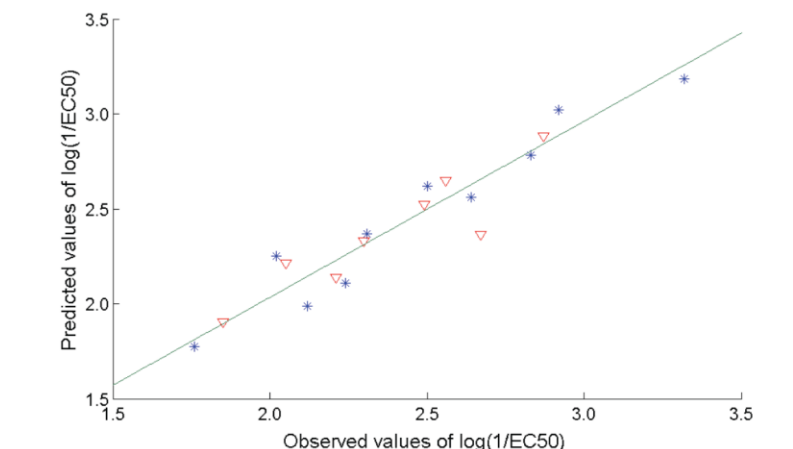


Figure 26. Experimentally determined versus predicted log values of $1/EC_{50}$. The straight line represents perfect agreement between experimental and calculated values. Squares represent values predicted for the metal oxides from the training set; triangles represent data calculated for metal oxides from the validation sets. The distance of each symbol from the green line corresponds to its deviation from the related experimental value.

Interestingly, the descriptors utilized in the nano-QSAR model (ΔH_f° and χ°) refer to the two types of processes, which collectively determine the toxicity of the metal oxide nanoparticles to the HaCaT cell line. The first process involves the detachment of metal cations from the surface of MeOx, whereas the second one is related to the surface redox activity of nanoparticles (transfer of electrons from the valence band to the conduction band is influenced by the intracellular redox processes occurring in the biological media). Both processes lead to the formation of highly reactive and less specific hydroxyl radicals, mainly responsible for inducing oxidative stress in the cells.

Mechanism I: Detachment of metal cations from the surface of MeOx: Metal cations (i.e., Cu^{2+}) released from the surface of MeOx nanoparticles may catalyze the formation of hydroxyl radicals (OH^\bullet) via so-called Haber-Weiss-Fenton cycle (18):



At any given time, reactive oxygen species (ROS), such as superoxide anion radicals ($O_2^{\bullet-}$), hydrogen peroxide (H_2O_2), and even highly reactive hydroxyl radicals (OH^\bullet) are being produced in all aerobic organisms as by-products of cellular respiration because

they use molecular oxygen to obtain energy (19). Indeed, superoxide anion radicals are products of one-electron reduction of the molecular oxygen (O_2):



Electrons required for the above reaction “leak” from the electron transport chain during cellular respiration (20,21). Hydrogen peroxide (H_2O_2) originates from various enzymatic reactions, including those catalyzed by the superoxide dismutases (SOD):



and the xanthine oxidase (XO) (19):



Then, superoxide anion radicals may react with hydrogen peroxide according to the Haber-Weiss reaction that leads to the formation of hydroxyl radicals:



However, most of the time, the cell is able to maintain a balance between the levels of oxidized and reduced species through various antioxidants and enzymes that scavenge the free radicals. Many of such species are constitutively present and have been highly conserved across evolution (22, 23). The non-enzymatic antioxidants include NADPH and NADH pools, β -carotene, ascorbic acid, mannitol, α -tocopherol, and glutathione (GSH). High concentrations of GSH help maintain a strong reducing environment in the cell, and its reduced form is governed by an enzyme that uses NADPH as its source of reducing power.

Problems arise when the cell is unable to maintain this balance due to increased ROS generation. When summarizing reactions (eq. 14) and (eq. 15), one can simply obtain the same reaction as (eq. 8), but this reaction is catalyzed by metal cations:



Thus, in the presence of metal cations released from the surface of MeOx nanoparticles, hydroxyl radicals can be formed much more extensively than normal. In effect, the concentration of highly reactive OH^\bullet radicals becomes too elevated for the natural scavengers to keep the physiological balance and the cell is overcome by the oxidative stress.

The first descriptor used in our nano-QSAR model (ΔH_f°) corresponds to the energy associated with a single metal-oxygen bond in the oxides ($E_{\Delta H^\circ}$) and the number of electrons involved in the formation reaction, since the standard enthalpy of formation ΔH_f° for a given MeOx can be expressed as (24):

$$E_{\Delta H^\circ} = - \frac{2 \cdot \Delta H_f^\circ \times 2.612 \times 10^{19}}{N_A \times n_e} \Rightarrow \Delta H_f^\circ = - \frac{n_e \times E_{\Delta H^\circ}}{\text{const.}} \quad (21)$$

Where: N_A is the Avogadro number and n_e is the number of electrons involved in the formation reaction. Thus, high absolute values of the enthalpy of formation of the cluster indicate metal oxide nanoparticles with strongly bound cations of large formal charge.

The second descriptor (χ^c) relates to properties of the cations themselves in the series of the studied oxides. According to Portier et al. (25), the value of electronegativity of a given metal oxide (χ) is strongly related to χ_+ - electronegativity of the corresponding cation (eq. 22):

$$C = 0.45 C_+ + 3.36 \quad (22)$$

The electronegativity χ_+ mainly depends on the ionic radius and formal charge of the cation. The highest values of χ_+ characterize those cations that have a relatively large charge distributed along a relatively small atomic radius. However, even if the formal charge is large, if it is distributed over a sizeable cationic volume (e.g. TiO_2), one should expect a lower value of the cation electronegativity (25). Since electronegativity describes the tendency to attract electrons, it is clear in the context of the Haber-Weiss-Fenton cycle that the increase of the cation electronegativity should result in the increase of catalytic properties of metal cations (metal cations are reduced, eq. 14) and consequently, increase the toxicity of the metal oxide nanoparticle.

Mechanism II: Redox properties of the metal oxides surface: The second mechanism is related to the ability of transferring electrons between the surface of MeOx and intracellular redox couples. This theory has been originally proposed by Burello and Worth (26, 27) and then extended by Zhang et al. (10). It states that the values of valence and conduction band energies (E_v and E_c) in relation to the standard redox potential (E°) of naturally occurring reactions in the cell could be the main factors

responsible for the toxicity of metal oxide nanoparticles (Figure 27). The most potentially toxic MeOx are those, for which E_c energy levels overlap with the standard redox potentials of the biologically vital redox couples (E° between -4.12 eV and -4.84 eV). For instance, TiO_2 nanoparticle (rutile) is capable of donating an electron for one-electron reduction of molecular oxygen (see eq. 5), because in this case $E^\circ = -4.30$ eV and E_c of TiO_2 is equal to -4.27 eV (28).

The current nano-QSAR model also supports this theory. Portier et al. (24) and Lide et al. (29) have defined a relationship between the standard enthalpy of metal oxide formation (ΔH_f°) and the band gap width E_g of the bulk material (eq. 23):

$$E_g = A \exp(0.34 \cdot \Delta H_f^\circ) \quad (23)$$

where A describes properties of the metal cation, depending on its location in the periodic table ($A = 1$ for d-block; $A = 0.8$ for s-block; $A = 1.35$ for p-block; and $A = 0.5$ for f-block elements). Note that for molecular clusters of the same size, the first descriptor employed in the nano-QSAR model (ΔH_f^c) is proportional to ΔH_f° . Thus, in such a case, ΔH_f^c is also expected to be related to the band gap width.

Similarly, the second descriptor (χ^c) corresponds to the Fermi level of the oxide (χ) that lies at the mid-point of the band gap (Figure 27). By involving two descriptors: ΔH_f^c and χ^c in the model equation, both energy levels: the conduction and valence band are represented.

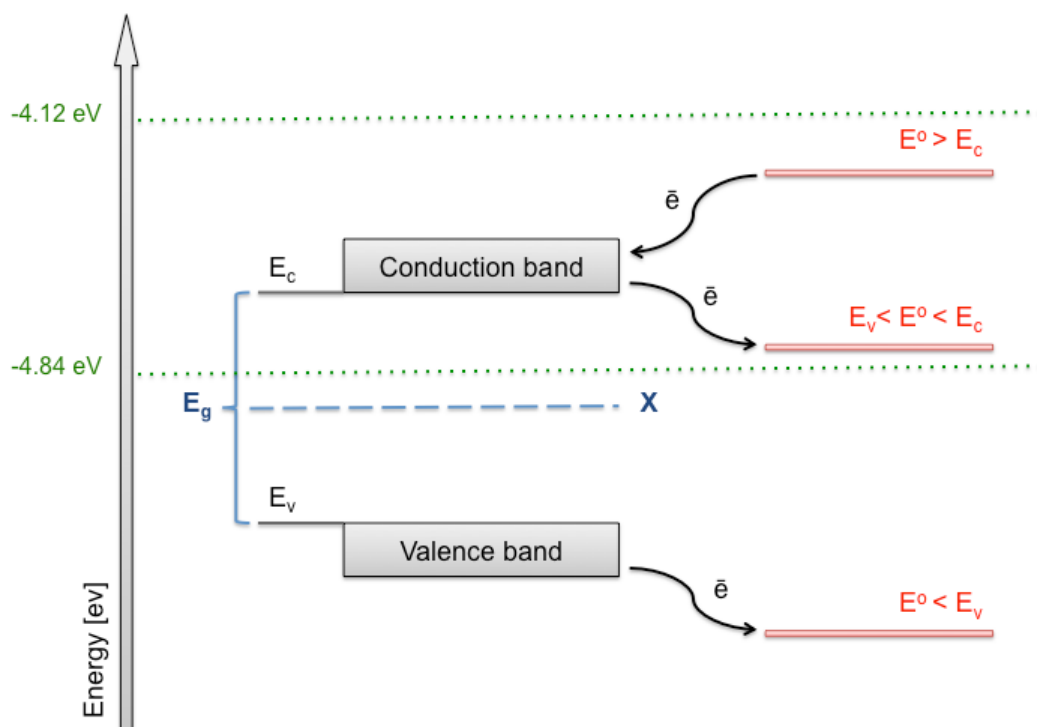


Figure 27. Mechanism of electron transfer between the MeOx surface and intracellular redox couples. The relative positions of the top of the valence band (E_v) and the bottom of the conduction band (E_c) with respect to the standard redox potential (E°) dictates, whether an electron transfer is feasible. Intracellular redox couples with E° above the conduction band can transfer electrons to the conduction band whereas redox couples having E° within the band gap (E_g) can accept electrons from the conduction band. The redox couples with E° below the valence gap can be only reduced by valence gap electrons. Symbol χ indicates electronegativity, which is related to the Fermi level for a given MeOx.

Which mechanism prevails?

There is no simple answer to this question. In our previous study on bacteria *E. coli* we were able to explain relative differences in toxicity within a set of 17 metal oxides by a model assuming only the first mechanism (see eq. 12). However, application of the same descriptor to the current data for human cells (HaCaT) does not provide satisfactory results. Similarly, Zhang et al. (10) postulated the second mechanism for explaining toxicity of metal oxides nanoparticles to human bronchial epithelial cells (BEAS-2B) and rat alveolar macrophage cells (RAW 264.7) and predicting them with a variety of *in silico* techniques. However, their predictions were incorrect for three important oxides: TiO_2 (false positive), CuO (false negative) and ZnO (false negative) – note that the model developed in our current study accurately predicts toxicity for these

three oxides in question. The authors concluded that high toxicity of CuO and ZnO is independent of their E_c levels and might be explained by their high solubility.

A detailed analysis of the recently published studies (10, 26, 28, 30) suggests that both mechanisms should be considered together, i.e. cytotoxicity of a nanoparticle can be induced by both mechanisms at the same time. There are three main factors governing the significance of contributions from the considered mechanisms in the particular case. These factors are: morphology of the cell, size of the nanoparticle and nanoparticle's solubility.

Bondarenko et al. (31) empirically confirmed that cytotoxicity of CuO nanoparticles to Gram-negative bacteria (*E. coli* and *P. fluorescens*) is Cu-cation dependent. But, the mechanism is very specific, regarding the morphology of Gram-negative bacteria cells. Gram-negative bacteria contain an additional outer membrane, which provides added protection against nanoparticles and other foreign bodies trying to invade the cell. The authors (31) noticed that copper ions (generated by Cu nanoparticles) were mainly stored in the space between the cytoplasmic membrane and the outer membrane, so-called periplasmic space. High concentrations of Cu ions lead to the formation of reactive oxygen species in the periplasm (see eq. 14 and 15). In turn, elevated concentrations of ROS in the periplasm results in leakage into the cytosol, where it continues to form additional ROS initiates an oxidative stress response. However, this mechanism is probably not relevant for eukaryotic cells that do not have an additional outer membrane and are capable of easily internalizing nanoparticles. Moreover, prokaryotes lack membrane bound organelles, including mitochondria, which is the site of cellular respiration in eukaryotes. Therefore the mitochondria are also an important source of intracellular ROS generation. In this case, electrons leak from the electron transport chain during respiration tract and react with molecular O_2 (see eq. 16).

This example illustrates the role of cell morphology and also explains the reason, why the same descriptors could not be used for modeling cytotoxicity of MeOx to *E. coli* and human HaCaT cell lines, even when the same or similar mechanism of cytotoxicity (Me-cation dependent) is considered. In the first case (model for *E. coli*) we have observed that toxicity of MeOx decreased in order: $Me^{2+} > Me^{3+} > Me^{4+}$, depending on the formal charge of the cation. In the case of HaCaT cell lines we did not observe such a relationship - the toxicity is related to the ratio between the formal charge and the atomic radius, not the formal charge itself. In addition, the energy of a single metal-oxygen bond is vital in the latter case. We postulate that the charge of metal cations plays a critical role in the transport of the cation to the periplasmic space in the bacteria cells. Since eukaryotic cells are capable of internalizing MeOx nanoparticles much easier, the process of ion detachment from the surface occurs inside the cell. In addition, redox activity of the surface itself (according to Mechanism II) may interrupt natural homeostasis of the cell processes.

Size of the nanoparticle is the second important factor. Many authors (32-34) reported a general trend: toxicity of MeOx increases with a decreasing size. This may be simply explained in the context of both proposed mechanisms. The total number of atoms at the nanoparticle surface scales with surface area divided by volume (i.e., for a spherical nanoparticle it scales as $N^{-1/3}$) (35). Moreover, atoms present at the surface are less

stable, since they are less coordinated (form less chemical bonds) than those in the nanoparticle's interior. Thus, they could be more easily detached from the surface (Mechanism I). In addition, very small nanoparticles behave more like a set of single molecules/atoms in a gas or liquid phase rather than as a bulk crystal. For example, the melting point of 2.5 nm Au nanoparticles is about 930 K, whereas the melting point for the bulk is 1336 K (36). When analyzing a plot of $N^{-1/3}$ function, one can conclude that differences in phys/chem properties, including redox properties (Mechanism II), should be especially significant for very small sizes, for which large fractions of atoms are present at the surface. That is why quantum dots are characterized by amazing properties, when compared with the bulk. However, with an increasing size, the properties of nanoparticles monotonically converge to the values observed for the bulk and become insignificant at sizes above 0.5-5 nm (dependent on the particular metal oxide). Interestingly, in our investigation, the descriptors of size derived from TEM images have not been selected by the genetic algorithm to the final nano-QSAR model. This means the variance in toxicity is explained mainly by the variance in surface properties (ΔH_f° and χ°) calculated for a set of the oxides based on molecular clusters representing fragments of the surface with a fixed size (0.5 × 0.5 × 0.5 nm). Thus, the influence of size on toxicity of the studied metal oxides in the HaCaT bioassay, if any, is minor, independently of the assumed mechanism.

As mentioned, Zhang et al. (10) suggest that high toxicity of CuO and ZnO nanoparticles is related to their relatively high solubility. The term 'solubility' however should be used in relation to nanoparticles with great precision. Dissolution of a nanoparticle is related to detachment of smaller fragments and dissociation of chemical bonds, which leads to the release of metal cations from the nanoparticle's surface. This, in fact, is in agreement with Mechanism I of inducing toxicity by MeOx. In that sense, for a given size, ΔH_f° might be employed as a measure of 'the ability of releasing metal cations', since it is proportional to energy of a single metal-oxygen bond in the oxides ($E_{\Delta H^\circ}$). As explained above, atoms present at the surface of a very small particle are less stable. Therefore, 'solubility' of nanoparticles may also be significantly size dependent. However, since in our study we used relatively large nanoparticles, such relationship has not been observed.

In conclusion, the present study combines experimental testing and computational modeling methodologies to reveal and explain the toxicity of nano-metal oxides to a human keratinocyte cell line. We have developed and validated an interpretative nano-QSAR model that reliably predicts toxicity of all considered compounds. It could be applied not only to NPs investigated in the current work, but also to unexplored related species, if they are located within its applicability domain. Finally, based on the present nano-QSAR investigation and the previously published nano-QSAR model (15), we discussed differences in the mechanisms of toxicity of MeOx nanoparticles to bacteria (prokaryotic system) and a human keratinocyte cell line (eukaryotic system). In both cases the exposure to MeOx NPs caused an increase in the generation of ROS *via* various mechanisms, which in turn lead to oxidative stress, and subsequent toxicity. Differences in the modes of toxic action occur mainly due to differences in the cells morphology, size of the nanoparticles and nanoparticles' solubility.

Materials and methods

Empirical toxicity testing

The Army Research Lab kindly provided the human keratinocyte cell line (HaCaT). The cells were grown in a T-75 flask with RPMI-1640 media (ATCC, Manassas, VA), supplemented with 10 % (v/v) fetal bovine serum (FBS, ATCC) and 1 % (w/v) penicillin/streptomycin (Sigma, St. Louis, MO), and incubated at 37 °C in a humidified incubator with 5 % CO₂.

Metal Oxide Nanoparticle Characterization

To verify morphology and size, one drop of a 100 µg/mL solution was spotted on a forever/carbon-coated TEM grid (EMS Diasum, Hatfield, PA) and allowed to dry. Once dried, the nanoparticles were viewed using a Philips/FEI CM200 TEM (Hillsboro, OR) at 120 kV.

Cellular Viability

Cell viability was measured using the CytoTox-Glo Cytotoxicity Assay from Promega (Madison, WI). This assay utilizes a luminogenic peptide substrate alanyl-alanyl-phenylalanyl-aminoluciferin (AAF-Glo) to measure dead cell protease activity from cells that have lost membrane integrity and is unable to penetrate the intact membrane of healthy cells. Cells were cultured in 96-well plates with 2.5×10^3 cells per well and allowed to grow at 37 °C with 5 % CO₂ for 24 h until ~80 % confluent. The cells were then exposed to varying concentrations of the MeOx for 24 h. After 24 h the cells were incubated with the AAF-Glo solution for 15 min at room temperature in the dark. The plate was read on a SpectraMAX GeminiXS microplate reader using the luminescence setting. Following the reading, lysis buffer (provided in the kit) was added to the plate and incubated an additional 15 min at room temperature in the dark. After 15 min the plate was re-read using the luminescence setting on the plate reader. Cell viability was determined using the following equation to normalize data for total cell number:

$$\text{Viable cell luminescence} = \frac{\text{Total luminescence (after lysis)} - \text{Experimental dead cell luminescence}}{\text{Experimental dead cell luminescence}}$$

The viable cell luminescence values were then compared to the control (cells without MeOx) and data was expressed as % control.

Statistical Analysis and Computational Modeling Methods

EC₅₀ values for all MeOx were extrapolated using the third order polynomial equation of the log transformed data with the least squares fit in GraphPad.

The metal oxides for which the both kinds of data (describing the toxicity and the structure) had been available were split into two sets: the training set (T) and the validation set (V). The training set was later used for developing the nano-QSAR model that involved selection of the most optimal complexity of the model (optimization step) and derivation of the model's formula (the calibration step). The validation set was

DISTRIBUTION A: Approved for public release; distribution unlimited, PA# 88ABW-2013-4142

utilized for the external validation of the model's performance to correctly predict toxicity of novel oxides - not involved in the model's optimization and calibration.

Molecular geometries of each cluster reflecting all characteristics of fragments of crystal structures (surface) of particular oxides, were optimized at the level of semi-empirical PM6 method (36) implemented in the MOPAC 2009 package (37). We calculated a pool of 16 quantum-mechanical descriptors reflecting variability of the nanoparticles' structure (Table 9). It is worth noting that the applicability of the PM6 method to nano-QSAR studies have been proved by our previous investigations (15).

Table 9. List of Calculated Quantum - Mechanical Descriptors

Metal oxide	ΔH_f°	TE	EE	Core	SAS	HOMO	LUMO	E_g	μ	E_v	E_c	χ^c	Hard	Shift	Ahof	Ad	Metal oxide
	kcal/mol	eV	eV	eV	Å ²	eV	eV	eV	eV	eV	eV	eV	eV	eV	Å ³	Å ³	
Al ₂ O ₃	-599.96	-2755.77	-11997.73	9241.96	307.16	-8.63	1.66	-10.28	-3.49	1.66	-8.63	3.49	5.14	-3.49	17.83	17.79	Al ₂ O ₃
Bi ₂ O ₃	-148.46	-2864.29	-11242.70	8378.42	251.06	-9.03	-1.65	-7.38	-5.34	-1.65	-9.03	5.34	3.69	-5.34	19.92	19.84	Bi ₂ O ₃
CoO	-786.82	-5378.20	-15466.67	20088.48	347.56	-9.21	-5.67	-3.55	-7.44	-5.67	-9.21	7.44	1.77	-7.44	32.50	31.50	CoO
Cr ₂ O ₃	-235.25	-2507.84	-10028.27	7520.43	167.30	-8.25	-0.46	-7.79	-4.36	-0.46	-8.25	4.36	3.89	-4.36	16.35	16.02	Cr ₂ O ₃
Fe ₂ O ₃	-378.54	-3480.89	-13651.60	10170.72	172.57	-8.33	-0.09	-8.24	-4.21	-0.09	-8.33	4.21	4.12	-4.21	12.33	12.32	Fe ₂ O ₃
In ₂ O ₃	-52.07	-1961.00	-6085.11	4124.10	191.20	-10.32	-3.25	-7.08	-6.78	-3.25	-10.32	6.78	3.54	-6.78	21.44	21.43	In ₂ O ₃
La ₂ O ₃	-157.72	-2686.12	-8602.36	6116.24	232.92	-10.91	-2.00	-8.90	-6.45	-2.00	-10.91	6.45	4.45	-6.45	4.95	4.95	La ₂ O ₃
Mn ₂ O ₃	-96.33	-6269.33	-34774.71	29505.38	321.38	-7.02	-2.98	-4.04	-5.00	-2.98	-7.02	5.00	2.02	-5.00	41.03	40.97	Mn ₂ O ₃
NiO	68.02	-4071.03	-22764.21	18093.18	179.35	-7.78	-1.16	-6.62	-4.47	-1.16	-7.78	4.47	3.31	-4.47	21.35	21.23	NiO
Sb ₂ O ₃	-206.73	-3804.78	-10756.33	18251.55	255.24	-7.96	-0.96	-7.00	-4.46	-0.96	-7.96	4.46	3.50	-4.46	23.21	23.12	Sb ₂ O ₃
SiO ₂	-618.26	-2764.16	-10201.74	7437.58	262.92	-7.90	0.28	-8.18	-3.81	0.28	-7.90	3.81	4.09	-3.81	31.58	31.54	SiO ₂
SnO ₂	-266.61	-3510.99	-17713.02	14202.02	359.32	-6.97	-2.18	-4.79	-4.57	-2.18	-6.97	4.57	2.40	-4.57	27.22	27.14	SnO ₂
TiO ₂	-1492.04	-2982.93	-12685.10	9902.17	271.58	-7.08	-2.73	-4.36	-4.91	-2.73	-7.08	4.91	2.18	-4.91	24.54	23.94	TiO ₂
V ₂ O ₃	-139.54	-3288.08	-7623.90	15455.81	206.12	-5.81	-0.66	-5.15	-3.24	-0.66	-5.81	3.24	2.58	-3.24	26.36	26.22	V ₂ O ₃
WO ₃	-715.43	-4310.92	-21750.82	17439.89	302.37	-10.39	-3.06	-7.33	-6.73	-3.06	-10.39	6.73	3.67	-6.73	24.16	23.79	WO ₃
Y ₂ O ₃	-135.28	-2179.76	-9171.06	6991.30	436.97	-4.05	-2.65	-1.40	-3.35	-2.65	-4.05	3.35	0.70	-3.35	54.00	53.98	Y ₂ O ₃
ZnO	-449.38	-1320.24	-3221.69	11901.45	153.42	-11.36	-5.30	-6.07	-8.33	-5.30	-11.36	8.33	3.03	-8.33	9.09	9.07	ZnO
ZrO ₂	-638.12	-3129.27	-3510.66	2179.39	178.99	-8.87	-1.03	-7.84	-4.95	-1.03	-8.87	4.95	3.92	-4.95	10.74	10.71	ZrO ₂

Based on the TEM microscopic images, we calculated a set of image descriptors reflecting the size distribution, shape, porosity, and surface area for all studied nanometer-sized metal and semimetal oxides. The procedure was as follows: we first converted the TEM pictures to numerical matrix in which each numerical value corresponded to a single pixel of the original picture. In the 8-bit monochrome image (called grayscale image) each pixel was assigned a value from 0-255. These values represent the image gray levels, and so conventionally it was assumed that 255 is the total blackness, while 0 represents the lowest level (the grey levels are the numbers in between). Thereafter, we defined image descriptors, for example, the surface area descriptor has been defined as the sum of all non-zero matrix elements, and the porosity descriptor has been estimated as the sum of the relative differences between the numerically expressed intensity of each pixel and its neighbors. We calculated the 11 image descriptors (Table 10).

Table 10. List of Calculated Image Descriptors

Metal oxide	A	V	$d_s = \sqrt{\frac{A}{\pi}}$	$d_{V/m} = \sqrt[3]{\frac{6V}{\pi}}$	$A_{R,S} = \frac{d_{min,S}}{d_{max,S}}$	$d_{savr} = \frac{6V}{A}$	$A_{R,Y} = \frac{d_{min,Y}}{d_{max,Y}}$	$P_x = \sum_{i=1}^n x_i - x_j $	$P_y = \sum_{i=1}^n y_i - y_j $	$\psi = \frac{\pi^{1/3} 6V^{2/3}}{A}$	$f_{circ} = \frac{4\pi A}{V^2}$	Metal oxide
	Area	Volume	Surface diameter	Volume/mass diameter	Volume/surface diameter	Aspect ratio X	Aspect ratio Y	Porosity X	Porosity Y	Sphericity	Circularity	
Al ₂ O ₃	1.11E+09	1.86E+06	1.88E+04	152.72	0.010	0.57	0.07	5.15E+04	-3.16E+05	6.62E-05	4.00E-03	Al ₂ O ₃
Bi ₂ O ₃	9.80E+08	2.05E+06	1.77E+04	156.52	0.013	0.40	0.07	-2.86E+05	-1.80E+05	7.94E-05	2.90E-03	Bi ₂ O ₃
CoO	1.11E+09	2.14E+06	1.90E+04	159.99	0.011	0.43	0.06	2.11E+04	-2.42E+05	7.07E-05	3.10E-03	CoO
Cr ₂ O ₃	8.72E+08	1.52E+06	1.87E+04	142.80	0.010	0.36	0.07	-3.42E+05	-5.51E+05	7.34E-05	4.70E-03	Cr ₂ O ₃
Fe ₂ O ₃	1.09E+09	1.83E+06	1.86E+04	150.43	0.010	0.45	0.07	-1.18E+05	-3.18E+05	6.52E-05	4.30E-03	Fe ₂ O ₃
In ₂ O ₃	1.07E+09	2.04E+06	1.85E+04	154.37	0.011	0.50	0.06	-1.68E+04	-2.81E+05	7.24E-05	3.92E-03	In ₂ O ₃
La ₂ O ₃	1.10E+09	1.91E+06	1.86E+04	153.90	0.011	0.52	0.07	1.33E+04	-2.87E+05	6.79E-05	3.80E-03	La ₂ O ₃
Mn ₂ O ₃	1.09E+09	2.04E+06	1.86E+04	157.34	0.011	0.48	0.06	7.57E+04	-2.46E+05	7.02E-05	3.60E-03	Mn ₂ O ₃
NiO	1.19E+09	1.96E+06	1.90E+04	155.28	0.010	0.60	0.07	6.55E+03	-3.11E+05	6.36E-05	3.90E-03	NiO
Sb ₂ O ₃	9.60E+08	1.80E+06	1.80E+04	150.86	0.011	0.24	0.06	3.49E+05	-3.72E+05	7.48E-05	3.70E-03	Sb ₂ O ₃
SiO ₂	9.71E+08	1.81E+06	1.76E+04	151.17	0.011	0.42	0.06	1.25E+05	-4.13E+05	6.92E-05	3.70E-03	SiO ₂
SnO ₂	9.99E+08	1.98E+06	1.72E+04	147.62	0.011	0.41	0.08	-6.23E+04	-3.28E+05	7.37E-05	3.60E-03	SnO ₂
TiO ₂	9.79E+08	1.80E+06	1.61E+04	150.06	0.012	0.41	0.07	9.79E+03	-2.98E+05	7.10E-05	3.70E-03	TiO ₂
V ₂ O ₃	1.30E+09	2.20E+06	2.13E+04	155.41	0.011	0.57	0.06	-5.81E+03	-2.50E+05	6.29E-05	3.40E-03	V ₂ O ₃
WO ₃	9.97E+08	1.92E+06	1.79E+04	153.75	0.011	0.41	0.07	-1.67E+05	-3.10E+05	7.11E-05	3.61E-03	WO ₃
Y ₂ O ₃	1.38E+09	2.26E+06	2.12E+04	162.86	0.011	0.63	0.05	1.02E+04	-1.89E+05	6.98E-05	3.93E-03	Y ₂ O ₃
ZnO	1.09E+09	1.95E+06	1.82E+04	154.98	0.011	0.54	0.06	1.83E+03	-3.04E+05	6.80E-05	3.70E-03	ZnO
ZrO ₂	1.16E+09	2.32E+06	1.92E+04	161.88	0.011	0.51	0.07	9.68E+03	-2.19E+05	6.86E-05	3.10E-03	ZrO ₂

The both types of descriptors (i.e. quantum-mechanical and image descriptors) have been auto-scaled, which means that the average value was subtracted from the descriptors and the resultant values were divided by the standard deviation to ensure the same scale and range of all variables.

For the modeling, we applied the multiple regression method combined with a genetic algorithm (GA-MLR). MLR is a standard regression technique in which the response y (toxicity) is expressed as a linear combination of independent variables x_i (descriptors), whereas GA is a mathematical procedure of independent variable selection that originates from Darwinian evolution theory. We applied a genetic algorithm to select the most efficient combination of the molecular descriptors for the MLR. In the first step, the algorithm generates a large number of random selections. More detailed explanation of genetic algorithms can be found elsewhere (37). We used the following steering parameters for the algorithm: the size of a population: 124, the percentage of the initial terms: 40%, the maximum number of generations: 100, the percentage of convergence: 50%, the mutation rate: 0.005, cross-over: double, the number of repetitions: 7. We obtained a statistically significant nano-QSAR model capable of successfully predicting the toxicity of the metal oxide nanoparticles to human keratinocyte cell line (HaCaT). Both the intercept and coefficients were significantly different from zero, based on the Student's t- test (Table 11).

Table 11. Statistics for the Model's Coefficients

		b_i	std. error	t-value	p-value
b_0	intercept	2.47	± 0.05	54.19	1.9×10^{-10}
b_1	coefficient	0.24	± 0.05	5.08	1.4×10^{-3}
b_2	coefficient	0.39	± 0.05	8.21	7.7×10^{-5}

References

- [1] Fujita K, et al. (2009) Gene expression profiles in rat lung after inhalation exposure to C 60 fullerene particles. *Toxicology* 258(1):47-55.
- [2] Handy RD, Owen R, Valsami-Jones E (2008) The ecotoxicology of nanoparticles and nanomaterials: Current status, knowledge gaps, challenges, and future needs. *Ecotoxicology* 17(5): 315-325.
- [3] Meng H, Xia T, George S, Nel AE (2009) A predictive toxicological paradigm for the safety assessment of nanomaterials. *ACS Nano* 3(7): 1620-1627.
- [4] Migdal C, et al. (2010) Internalisation of hybrid titanium dioxide/para-amino benzoic acid nanoparticles in human dendritic cells did not induce toxicity and changes in their functions. *Toxicol Lett* 199(1): 34-42.
- [5] Nel AE, et al. (2009) Understanding biophysicochemical interactions at the nano-bio interface. *Nat Mater* 8(7): 543-557.
- [6] Park S, Chibli H, Wong J, Nadeau JL (2011) Antimicrobial activity and cellular toxicity of nanoparticle-polymyxin B conjugates. *Nanotechnology* 22(2011): 185101. doi:10.1088/0957-4484/22/18/185101.
- [7] Shvedova AA, Pietroiusti A, Fadeel B, Kagan VE (2012) Mechanisms of carbon nanotube-induced toxicity: Focus on oxidative stress. *Toxicol Appl Pharmacol* 261(2): 121-133.
- [8] Zhang H, et al. (2012) Use of Metal Oxide Nanoparticle Band Gap To Develop a Predictive Paradigm for Oxidative Stress and Acute Pulmonary Inflammation. *ACS Nano* 6(5): 4349-4368.
- [9] Rivera Gil P, Oberdörster G, Elder A, Puentes V, Parak WJ (2010) Correlating physico-chemical with toxicological properties of nanoparticles: the present and the future. *ACS Nano* 4(10): 5527-5531.
- [10] Jiang J, Oberdörster G, Biswas P (2009) Characterization of size, surface charge, and agglomeration state of nanoparticle dispersions for toxicological studies. *J Nanopart Res* 11(1): 77-89.
- [11] Powers KW, Palazuelos M, Moudgil BM, Roberts SM (2007) Characterization of the size, shape, and state of dispersion of nanoparticles for toxicological studies. *Nanotoxicology* 1(1): 42-51.
- [12] Gajewicz A, et al. (2012) Advancing risk assessment of engineered nanomaterials: Application of computational approaches. *Adv Drug Delivery Rev* 64(15): 1663-1693.
- [13] Puzyn T, et al. (2011) Using nano-QSAR to predict the cytotoxicity of metal oxide nanoparticles. *Nat Nanotechnol* 6(3): 175-178.
- [14] OECD, in 37th Joint Meeting of the Chemicals Committee and Working Party on Chemicals, Pesticides and Biotechnology. (Organisation for Economic Co-Operation and Development, Paris, France, 2004).

DISTRIBUTION A: Approved for public release; distribution unlimited, PA# 88ABW-2013-4142

- [15] Gramatica P (2007) Principles of QSAR models validation: internal and external. *QSAR Comb Sci* 26(5): 694-701.
- [16] Stohs SJ, Bagchi D (1995) Oxidative mechanisms in the toxicity of metal ions. *Free Radical Biol Med* 18(2): 321-336.
- [17] Halliwell B, Gutteridge JM (1999) *Free Radicals in Biology and Medicine*. (Oxford University Press, Oxford, UK).
- [18] Ames BN, Shigenaga MK, Hagen TM (1993) Oxidants, antioxidants, and the degenerative diseases of aging. *Proc Natl Acad Sci* 90(17): 7915-7922.
- [19] Turrens JF (2003) Mitochondrial formation of reactive oxygen species. *J Physiol* 552(Pt 2): 335-344.
- [20] Imlay JA (2008) Cellular defenses against superoxide and hydrogen peroxide. *Annu Rev Biochem* 77: 755-776.
- [21] Cabiscol E, Piulats E, Echave P, Herrero E, Ros J (2000) Oxidative stress promotes specific protein damage in *Saccharomyces cerevisiae*. *J Biol Chem* 275(35): 27393-27398.
- [22] Portier J, et al. (2004) Thermodynamic correlations and band gap calculations in metal oxides. *Prog Solid State Chem* 32(3-4): 207-217.
- [23] Portier J, Campet G, Poquet A, Marcel C, Subramanian MA (2001) Degenerate semiconductors in the light of electronegativity and chemical hardness. *Int J Inorg Mater* 3(7): 1039-1043.
- [24] Burello E, Worth AP (2011) A theoretical framework for predicting the oxidative stress potential of oxide nanoparticles. *Nanotoxicology* 5(2): 228-235.
- [25] Burello E, Worth AP (2011) QSAR modeling of nanomaterials. *Wiley Interdiscip Rev Nanomed Nanobiotechnol* 3(3): 298-306.
- [26] Burello E, Worth AP (2012) in *Towards Efficient Designing of Safe Nanomaterials: Innovative Merge of Computational Approaches and Experimental Techniques* J. Leszczynski, T. Puzyn, Eds. (Royal Society of Chemistry).
- [27] Lide DR (2006) *CRC Handbook of Chemistry and Physics*. (Taylor & Francis, Boca Raton, Florida).
- [28] Linkov I, et al. (2009) Emerging methods and tools for environmental risk assessment, decision-making, and policy for nanomaterials: summary of NATO Advanced Research Workshop. *J Nanopart Res* 11(3): 513-527.
- [29] Bondarenko O, Ivask A, K  inen A, Kahru A (2012) Sub-toxic effects of CuO nanoparticles on bacteria: Kinetics, role of Cu ions and possible mechanisms of action. *Environ Pollut* 169(2012): 81-89.
- [30] Carlson C, et al. (2008) Unique cellular interaction of silver nanoparticles: Size-dependent generation of reactive oxygen species. *J Phys Chem B* 112(43): 13608-13619.

- [31] Prabhu BM, Ali SF, Murdock RC, Hussain SM, Srivatsan M (2010) Copper nanoparticles exert size and concentration dependent toxicity on somatosensory neurons of rat. *Nanotoxicology* 4(2): 150-160.
- [32] Kumari M, et al. (2012) Repeated oral dose toxicity of iron oxide nanoparticles: Biochemical and histopathological alterations in different tissues of rats. *J Nanosci Nanotechnol* 12(3): 2149-2159.
- [33] Roduner E (2006) Size matters: why nanomaterials are different. *Chem Soc Rev* 35(7): 583-592.
- [34] Koga K, Ikeshoji T, Sugawara KI (2004) Size- and temperature-dependent structural transitions in gold nanoparticles. *Phys Rev Lett* 92(11): 115507-115511.
- [35] Stewart JJP (2007) Optimization of parameters for semiempirical methods V: modification of NDDO approximations and application to 70 elements. *J Mol Model* 13(12): 1173-1213.
- [36] Stewart JJP (2009) *S. C. Chemistry*, Ed. Available from: <http://openmopac.net/MOPAC2009.html> (accessed April 02, 2012).
- [37] Holland J (1992) *Adaptation in Natural and Artificial Systems*. (MIT Press, Michigan).

C. Conduct an Expert Review of AFSG/SG9R Nanomaterial Research Plan

Submitted as an independent report.

D. Conduct a Literature Search, Review, and Assessment

Submitted as an independent report.

E. Develop a Framework for the Interaction Between Predictive, Computational, and Other Relevant Models and a Database (s)

Submitted as an independent report.

Budget

Labor:	\$310,000	
Travel/TDY:	\$7,000	Expert Review Panel
Supplies:	\$5,000	
Equipment:	\$98,000	<ul style="list-style-type: none"> • 3936NL76 NRC Scanning Mobility Particle Sizer \$ 90,000 • 3089 Nanometer Aerosol Sampler \$9,762.98 • 390069 Data Merge Software \$1,500.00
Computers:	0	
ODCs:	\$70,000	Contracted database development
Fee:	0	
Other:	0	
Total:	\$490,000.00	

Publications

A. ACCEPTED PUBLICATIONS:

Mukhopadhyay A, Grabinski CM, Saleh N, Hussain SM. Effect of surface chemistry of gold nanospheres on protein adsorption and cell uptake in vitro. Applied Biochemistry and Biotechnology, 2012; 167, 327-37.

Schaeublin NM, Braydich-Stolle LK, Maurer EI, Park KW, MacCuspie RI, Afrooz ARMN, Saleh NB, Vaia RA, Hussain SM. Does shape matter: Bioeffects of gold nanomaterials in a human skin cell model. Langmuir 2012; 28, 3248-58.

Sharma M, Salisbury RL, Maurer E., Hussain SM and Sulentic CEW (2011) Gold nanoparticles induce transcriptional activity of NF- κ B in a B-lymphocyte cell line. Nanoscale 2013; 5, 3747.

B. SUBMITTED PUBLICATIONS:

Grabinski C, Salaklang, Garrett C, Schrand A, Hussain S, Hofmann H. Multi-functionalized SPIONs for Nuclear Targeting Applications. Submitted to Nano.

Schaeublin NM, Maurer EI, Gajewicz A, Puzyn T, Leszczynski J, and Hussain SM. Application of QSAR Modeling to Predict Metal Nanoparticle Toxicity. In progress. Submitted to PNAS.

C. PUBLICATIONS IN PREPARATION:

Grabinski C, Wang T, Kah J, Hamad-Schifferli K, Hussain S. Stability, Toxicology, And Uptake Of Amphiphilic Ligand-Coated Gold Nanorods. In Progress; to be submitted to Nanoletters.

Grabinski C, Wang T, Kah J, Hamad-Schifferli K, Hussain S. Stability, Toxicology, And Uptake Of Amphiphilic Ligand-Coated Gold Nanorods. In Progress; to be submitted to Nanoletters.

D. ABSTRACTS AND PRESENTATIONS

- Grabinski C, Sankaran M, Hussain SM. *Realistic Assessment of Nanomaterial Toxicity In Vitro using a Nanoaerosol Exposure Chamber: Poster presented at: Society of Toxicology Annual Meeting; 2013 Mar 12; San Antonio, TX.*
- Grabinski C, Kah J, Hamad-Schifferli K, Hussain S. *Protein Adsorption and Cellular Response of Gold Nanorods Coated with Amphiphilic Ligands. Poster presented at: Nanotechnology for Defense. 2012 August 6; Las Vegas, NV.*
- Kah J, Grabinski C, A. Zubieta, R. Saavedra, Hussain S, Hamad-Schifferli K. *Protein adsorption and types of amphiphilic ligands coated on gold nanorods affect their stability and cellular response. Talk presented at: EMRS, 2012 May 15; Strasbourg, France.*
- Grabinski C, Sankaran M, Hussain SM. *Design of an In Vitro Chamber to Study Realistic Occupational Exposure of Engineered Nanomaterials: Poster presented at: Toxicology and Risk Assessment; 2012 May 2; West Chester, OH. *Earned Best Abstract and Best Poster Awards.*
- Grabinski C, Sankaran M, Hussain SM. *Design of an In Vitro Chamber to Study Realistic Occupational Exposure of Engineered Nanomaterials: Poster presented at: Society of Toxicology Annual Meeting; 2012 Mar 13; San Francisco, CA.*
- Schaeublin NM, Maurer EI, Gajewicz A, Puzyn T, Leszczynski J, and Hussain SM. *Application of QSAR Modeling to Predict Metal Nanoparticle Toxicity. Poster presented at: Society of Toxicology Annual Meeting; 2012 Mar 13; San Francisco, CA.*
- Grabinski C, Sankaran M, Hussain SM. *Design of an In Vitro Chamber for Occupational Exposure Assessment of NMs: 2012 Jan 10; Talk presented at: ENM EHS meeting; Dayton, OH.*
- Grabinski C, Sankaran M, Hussain SM. *In Vitro Chamber to Study Realistic Occupational Exposure of Engineered Nanomaterials to Biological Systems. Poster session presented at: Ohio Valley Society of Toxicology: 2011 September 19; Dayton, OH.*
- Turner B, Grabinski C, Hussain S. *Kinetics of Fluorescent Nanoparticles in an Airway Tissue Model. Poster session presented at: Human Effectiveness Summer Intern Research Presentation Day; 2011 Aug 16; Dayton, OH.*
- Grabinski C, Sankaran M, Hussain SM. *Portable In Vitro Chamber to Study Realistic Occupational Exposure of Engineered Nanomaterials to Biological Systems. Poster session presented at: Air Force Medical Services Conference: 2011 August 1-4; Washington D.C.*